

Multi-functional metal–organic frameworks assembled from a tripodal organic linker†

Sérgio M. F. Vilela,^{ab} Duarte Ananias,^a Ana C. Gomes,^a Anabela A. Valente,^a Luís D. Carlos,^c José A. S. Cavaleiro,^b João Rocha,^a João P. C. Tomé^b and Filipe A. Almeida Paz^{*a}

Received 20th April 2012, Accepted 21st June 2012

DOI: 10.1039/c2jm32501b

The reaction between (benzene-1,3,5-triyltris(methylene))triphosphonic acid (H₆bmt) and lanthanide chlorides, under typical hydrothermal conditions (180 °C for 3 days) or using microwave heating (5 minutes above 150 °C), led to the isolation of an isotypical series of compounds formulated as [Ln₂(H₃bmt)₂(H₂O)₂]·H₂O [where Ln³⁺ = La³⁺ (**1**), Ce³⁺ (**2**), Pr³⁺ (**3**), Nd³⁺ (**4**), (La_{0.95}Eu_{0.05})³⁺ (**5**) and (La_{0.95}Tb_{0.05})³⁺ (**6**)]. Compounds **1** to **4** have been readily isolated as large single-crystals and their structures determined in the monoclinic *C2/c* space group using single-crystal X-ray diffraction. All compounds were thoroughly characterized in the solid-state using powder X-ray diffraction, FT-IR spectroscopy, thermogravimetry, scanning electron microscopy (SEM and EDS) and elemental analysis. Solid-state NMR (³¹P MAS and ¹³C{¹H} CP MAS) and thermodiffraction studies have been performed on the La³⁺-based material. [Ln₂(H₃bmt)₂(H₂O)₂]·H₂O were found to be three-dimensional frameworks with water molecules (both of crystallization and coordinated to the lanthanide center), which could be reversibly removed by either heating the materials or by applying high vacuum. This typical zeolitic behaviour was confirmed experimentally by determining the crystal structure of the evacuated La³⁺-based material (**1-dehyd**) using single-crystal X-ray diffraction. This series of materials was found to exhibit dual functionality: photoluminescence and catalytic activity. Small amounts (5%) of Eu³⁺ and Tb³⁺ cations were engineered into the La³⁺-based matrices, promoting the isolation of optically active materials. The H_{6-x}bmt^{x-} residues were found to be good sensitizers of Tb³⁺, with **6** having the remarkable absolute emission quantum yield of *ca.* 46% (at 280 nm excitation). The zeolitic properties of the Eu³⁺-based material allowed an increase of the quantum efficiency from *ca.* 15% to 54% by removing under vacuum all water molecules in the material. Based on studies of the La³⁺-based material, these compounds can be employed as effective heterogeneous catalysts in the ring-opening reaction of styrene oxide with methanol, showing excellent regioselectivity, recyclability and structural stability in consecutive catalytic runs.

1. Introduction

Metal–Organic Frameworks (MOFs) are hybrid crystalline materials assembled from metals (or clusters of metals) interconnected by way of polytopic organic linkers into multi-dimensional networks. In this context, design principles of

MOFs rely solely on a careful selection of metals and ligands and on the employed synthetic method that will be used to promote crystallization.¹ Research in the field of MOFs is still growing, being motivated by either their unique and peculiar structural architectures² or by their potential industrial applications.³ Indeed, MOFs, particularly those exhibiting permanent porosity,

^aDepartment of Chemistry, CICECO, University of Aveiro, 3810-193 Aveiro, Portugal. E-mail: filipe.paz@ua.pt; Fax: +351 234 370084; Tel: +351 234 247126

^bDepartment of Chemistry, QOPNA, University of Aveiro, 3810-193 Aveiro, Portugal

^cDepartment of Physics, CICECO, University of Aveiro, 3810-193 Aveiro, Portugal

† Electronic supplementary information (ESI) available: Additional crystallographic information: crystal structures in CIF format. Liquid state characterization of *L*³⁺ and H₆bmt: ¹³C spectrum of *L*³⁺; ¹H, ¹³C and ³¹P spectra of H₆bmt. Electron microscopy studies: EDS mapping and quantification of the various elements constituting the

mixed-lanthanide materials. Solid-state NMR studies: ¹³C{¹H} and ³¹P HPDEC spectra of [La₂(H₃bmt)₂(H₂O)₂]·H₂O (**1**). FT-IR spectra of bulk **1** to **6** materials. Thermograms of compounds **2** to **6**. Additional photoluminescence data: ⁵D₀ decay curve lifetimes of the as-prepared and dehydrated Eu³⁺-containing material; excitation and emission spectra, and lifetime calculations for the Tb³⁺-containing material; excitation and emission spectra, and fluorescence and phosphorescence calculations for the La³⁺-containing material; theoretical considerations used to calculate the theoretical quantum efficiency and the number of coordinated water molecules. CCDC 846598–846602. For ESI and crystallographic data in CIF or other electronic format see DOI: 10.1039/c2jm32501b

find nowadays a multitude of potential uses or applications in industry or in devices. They can be employed in the selective adsorption or separation of gases or molecules (*e.g.*, separation of CO₂ from CH₄, selective adsorption of H₂, separation of propane from propene),⁴ in the preparation of thin films or membranes,⁵ in medical applications (*e.g.*, drug delivery, contrasting agents),⁶ in photoluminescent or magnetic materials,^{5c,6a,7} as heterogeneous catalysts,⁸ in conductive materials,^{7h,9} among others.

Even though the vast majority of MOFs are based on *d*-block or main group elements bound to carboxylate- or pyridine-based groups,¹⁰ metal centers such as lanthanides¹¹ and distinct organic chelating groups (such as phosphonates or sulfonates)¹² are now becoming a topical area of research. Lanthanides are of great importance: on the one hand, structurally their high coordination numbers and predictable ionic radii reduction along the series may lead to fascinating framework architectures and modulation;¹¹ on the other hand, their photophysical properties permit the engineering of functional photoluminescent materials.^{7a} Contrasting with, for example, carboxylates, phosphonate groups can easily mimic the tetrahedral building blocks of zeolites, having three terminal oxygen atoms able to chelate to a multitude of metallic centres through stronger bonds than carboxylate groups. This can further lead to more stable networks.

Following our on-going research efforts to design and prepare novel functional MOF materials based on lanthanide centers (hereafter denominated as LnOFs),^{7a,13} and specifically designed organic linkers,¹⁴ particularly with phosphonate groups, we report in this paper a new family of dual functional (photoluminescent and catalytic) non-porous (*i.e.*, compact) materials formulated as [Ln₂(H₃bmt)₂(H₂O)₂]·H₂O [where Ln³⁺ = La³⁺ (**1**), Ce³⁺ (**2**), Pr³⁺ (**3**), Nd³⁺ (**4**), (La_{0.95}Eu_{0.05})³⁺ (**5**) and (La_{0.95}Tb_{0.05})³⁺ (**6**)], based on the tripodal (benzene-1,3,5-triyltris(methylene)triphosphonic acid (H₆bmt) organic linker. Both this molecule and its trimethylated form have been previously reported in a handful of structures,¹⁵ but only the recent structure reported by Yang *et al.* with H_{6-x}bmt^{x-} residues corresponds to a true MOF architecture: [Cu₃(bmt)(H₂O)_{3,6}]·H₂O.^{15c} The [Ln₂(H₃bmt)₂(H₂O)₂]·H₂O system herein reported constitutes, therefore, to the best of our knowledge, the first example of robust lanthanide-containing photoluminescent 3D networks assembled from tripodal H_{6-x}bmt^{x-} residues. We show that [Ln₂(H₃bmt)₂(H₂O)₂]·H₂O materials can be readily isolated as large single-crystals by hydrothermal or microwave-assisted synthesis, and that the water molecules (both of crystallization and coordinated) housed within the structure can be readily removed (*i.e.*, materials exhibit a typical zeolitic behaviour). This process was shown to occur in a typical single-crystal-to-single-crystal fashion, being accompanied structurally by single-crystal X-ray diffraction studies (for **1**) and using photoluminescence investigations (for **5** and **6**). Optically active compounds have been prepared by engineering into La³⁺ matrices Eu³⁺ and Tb³⁺ cations, leading to materials capable of converting UV radiation into visible light, some with high quantum yields (for Tb³⁺). [La₂(H₃bmt)₂(H₂O)₂]·H₂O was also found to be a highly regioselective, reusable and structurally robust heterogeneous catalyst in the ring-opening reaction of styrene oxide with methanol giving 2-methoxy-2-phenylethanol as the only product, under relatively mild conditions, in 80% yield after 24 h of reaction.

2. Results and discussion

2.1. Ligand design strategy

For the last few years, we have been interested in the preparation and study of functional MOF materials based on flexible tripodal organic linkers (employed as primary building units – PBUs). In this context, we have been progressively replacing carboxylic acid groups with phosphonic acid groups, and have described a number of families of structures based on nitrilotriacetic acid,¹⁶ *N*-(phosphonomethyl)iminodiacetic acid,^{13b,17} *N*-(carboxymethyl)iminodi(methylphosphonic acid)¹⁸ and nitrilotris(methylene-phosphonic acid)^{13a,19} (Scheme 1). These previous investigations led us to the following conclusions:

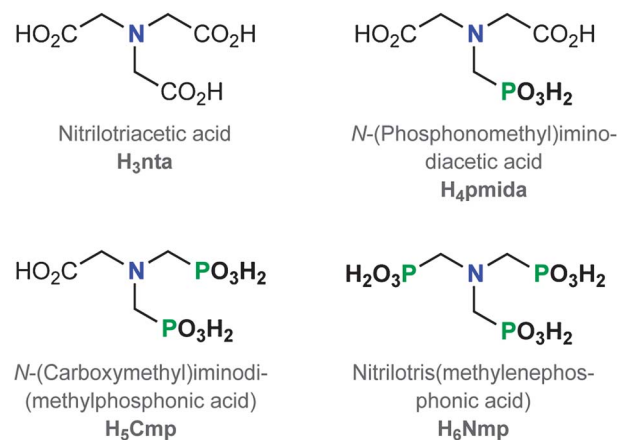
(i) The central nitrogen atom core, despite being a suitable moiety to employ in divergent tripodal organic PBUs, also promotes a high degree of flexibility of the ligand and consequently supramolecular isomerism; this may be the reason why, typically, we isolate microcrystalline MOF powders;

(ii) Layered materials are usually isolated because the organic PBUs act as chelating agents of the metal cations and branching is only facilitated in two directions of the space;

(iii) Because many of these previously reported structures contain *f*-block elements, we observed that the absence of suitable sensitizers in the organic PBUs (*e.g.*, aromatic rings) led to poor photoluminescent properties. To boost emission of the isolated lanthanide–organic frameworks (LnOFs) specific groups have to be included, such as aromatic rings, so as to promote an effective *antenna effect*;

(iv) In addition, the central nitrogen atom appears protonated in the synthesized MOF structures (as also occurs in the zwitterionic forms of the starting organic PBUs), which constitutes an additional quencher (non-radiative) of the photoluminescent properties.

The inclusion of aromatic moieties by the removal of the central nitrogen atom (in blue in Scheme 1) appeared to us as the next logical step in our pursuit to design more efficient photoluminescent LnOFs.^{7a} Applying these considerations to nitrilotris(methylenephosphonic acid), which we recently employed in the development of a new photoluminescent and



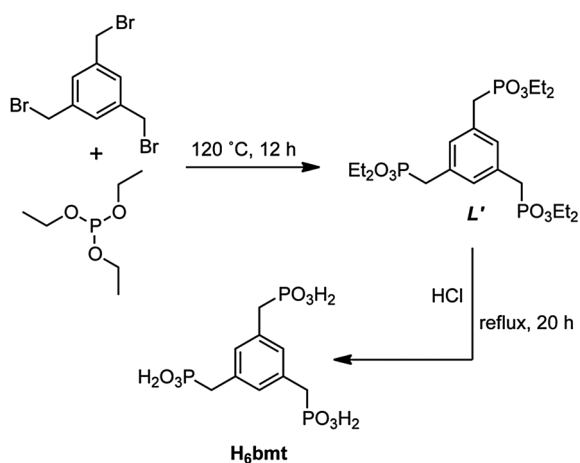
Scheme 1 Flexible tripodal organic ligands based on carboxylic and/or phosphonic acid groups previously used by our group for the preparation of MOF materials.

catalytic system,^{13a} we obtain the linker (benzene-1,3,5-triyltris(methylene))triphosphonic acid (H_6bmt): while retaining the high flexibility associated with the pendant $-CH_2-$ moieties, structural rigidity is also concomitantly increased due to the central benzene ring.

The crystal structure of H_6bmt was reported nearly a decade ago by Jaffrès *et al.*,^{15a} but this molecule has been scarcely employed in either the synthesis of coordination-based complexes or in traditional Crystal Engineering approaches: the research group of Clearfield^{15b} has successfully used H_6bmt in the solvothermal (water–ethanol mixture as the solvent) preparation of dimeric complexes of Cu^{2+} , $[Cu_2(H_4bmt)_2(4,4'-bpy)(H_2O)_2]$; it was also employed in the construction of a supramolecular network extensively studied by X-ray diffraction and solid-state NMR by the research groups of Montouillout and Jaffrès;^{15a} only recently the first MOF structure with Cu^{2+} was reported by Yang *et al.*^{15c} It is interesting to emphasize that the trimethylated derivative of H_6bmt , ((2,4,6-trimethylbenzene-1,3,5-triyl)tris(methylene))tris(phosphonic acid), has also been scarcely studied: besides the reports of a dimeric complex with Ce^{3+} ,^{15c} and another describing the crystal structure of its monohydrated form,^{15d} only the same work of Yang *et al.*^{15c} shows some progress in the use of this linker to prepare a Cu^{2+} supramolecular cage and a Co^{2+} -MOF structure.

2.2. Preparation of (benzene-1,3,5-triyltris(methylene))triphosphonic acid

(Benzene-1,3,5-triyltris(methylene))triphosphonic acid (H_6bmt) was prepared by a two-step reaction according to published procedures with small modifications (Scheme 2).²⁰ Synthesis of H_6bmt started with a Michaelis–Arbusov reaction of 1,3,5-tris(bromomethyl)benzene²¹ with triethyl phosphite at 120 °C. Upon completion of the reaction the excess of triethyl phosphite was removed by distillation under reduced pressure. The intermediate compound L' [hexaethyl(benzene-1,3,5-triyltris(methylene))tris(phosphonate)] was purified by flash column chromatography and isolated as a colorless oil in excellent yield (88%). The second step was an acid hydrolysis reaction: L' was treated with 6 M HCl, for 20 h at reflux, and H_6bmt was



Scheme 2 Two-step reaction procedure for the preparation of (benzene-1,3,5-triyltris(methylene))triphosphonic acid (H_6bmt).

immediately isolated as a white crystalline solid in 92% yield. H_6bmt and the intermediate L' were, when possible, characterized by spectroscopic (see Materials and methods section) and X-ray diffraction techniques. Data were compared, whenever available, with published data: the 1H and ^{31}P spectra of the intermediate L' are readily available in the literature and are in agreement with the data obtained by us;^{20a,22} the crystal structure of H_6bmt was described at ambient temperature nearly a decade ago by Jaffrès *et al.*^{15a} and agrees well with our low temperature determination (data not shown). As ESI to this paper we provide the ^{13}C spectrum of L' (Fig. S1†) and the full liquid characterization of H_6bmt (1H , ^{13}C and ^{31}P spectra in Fig. S2 to S4†).

2.3. Synthesis of LnOFs and bulk characterization

Hydrothermal synthesis and the quest for milder synthetic conditions. The reaction between (benzene-1,3,5-triyltris(methylene))triphosphonic acid (H_6bmt) and lanthanide(III) chloride hydrates which afforded $[Ln_2(H_3bmt)_2(H_2O)_2] \cdot H_2O$ materials as large single crystals [where $Ln^{3+} = La^{3+}$ (1), Ce^{3+} (2), Pr^{3+} (3), Nd^{3+} (4), $(La_{0.95}Eu_{0.05})^{3+}$ (5) and $(La_{0.95}Tb_{0.05})^{3+}$ (6)] occurred under typical hydrothermal conditions at a temperature of 180 °C, under autogeneous pressure, over a period of 3 days (for additional details see the dedicated Materials and methods section). The structural features of these materials could, therefore, be readily unveiled using single-crystal X-ray diffraction studies as described in the following subsection. Independent of the lanthanide (or a mixture of lanthanides for the optically active materials 5 and 6), these conditions were highly

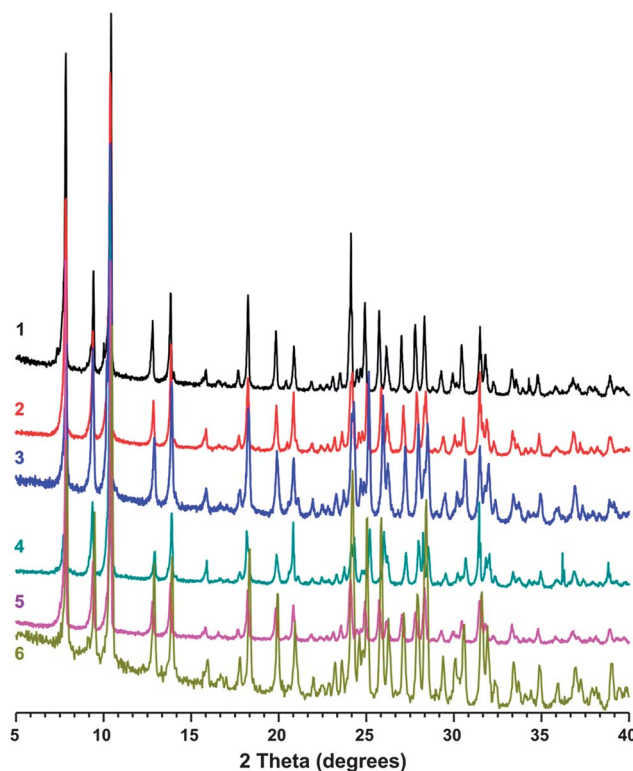


Fig. 1 Powder X-ray diffraction patterns for the bulk $[Ln_2(H_3bmt)_2(H_2O)_2] \cdot H_2O$ materials [where $Ln^{3+} = La^{3+}$ (1), Ce^{3+} (2), Pr^{3+} (3), Nd^{3+} (4), $(La_{0.95}Eu_{0.05})^{3+}$ (5) and $(La_{0.95}Tb_{0.05})^{3+}$ (6)].

reproducible, systematically yielding crystalline products of the desired phases. Phase purity and homogeneity of the bulk samples **1** to **6** have been confirmed by using in tandem powder X-ray diffraction (Fig. 1), FT-IR spectroscopy, and elemental composition and electron microscopy analyses.

Aiming to investigate if milder conditions could be employed, the preparation of $[\text{La}_2(\text{H}_3\text{pmt})_2(\text{H}_2\text{O})_2] \cdot \text{H}_2\text{O}$ (**1**) was further investigated at 100 °C for reaction times ranging from 1 to 3 days. As assessed from powder X-ray diffraction studies (Fig. 1), the desired pure phase could be readily isolated under all the tested conditions as large single-crystals (Fig. S5 in the ESI†). These studies led to the conclusion that these materials can indeed be isolated under very mild conditions, which is attractive in terms of process economy (reduced energy consumption and operation costs).

Following our interest in the use of faster and cleaner reaction methods in the preparation of MOFs, the synthesis of $[\text{La}_2(\text{H}_3\text{pmt})_2(\text{H}_2\text{O})_2] \cdot \text{H}_2\text{O}$ (**1**) was also tested using microwave irradiation (see dedicated Materials and methods section for additional details). For reaction periods of 5 minutes, compound **1** could only be isolated as a pure phase for temperatures greater than 150 °C, also as large single-crystals having the same crystal habit as that obtained from conventional hydrothermal synthesis (ascertained by powder X-ray diffraction and SEM images – data not shown).

Crystal engineering of optically active materials. Optically active materials containing Eu^{3+} and Tb^{3+} embedded into La^{3+} matrices (see detailed photophysical studies in Subsection 2.5) were also isolated as bulk microcrystalline materials by including in the reactive gels 5% of Eu^{3+} or Tb^{3+} salts (in mol; see Materials and methods section for details). We note that this methodology of preparing optically active materials permits, on the one hand, to guarantee that the framework structure is not altered due to the known lanthanide contraction effect and, on the other hand, that Eu^{3+} and Tb^{3+} cations are statistically diluted in the networks so as to prevent self-quenching effects.

Despite the fact that crystal morphology remains approximately identical with the inclusion of Eu^{3+} and Tb^{3+} , the overall crystallite size of the products was slightly reduced when compared with the single lanthanide phases. Additionally, crystals were also isolated as twinned aggregates (Fig. S6 and S7 in the ESI†). EDS quantification (not shown) and mapping studies clearly show that (i) both the Eu^{3+} and Tb^{3+} cations were included in the prepared LnOFs and that (ii) the distribution of these elements is completely random in the materials.

Solid-state NMR and FT-IR spectroscopy. As in our previous studies of LnOFs containing the flexible *N*-(carboxymethyl)iminodi(methylphosphonic acid)¹⁸ and nitrilotris(methylene-phosphonic acid)^{13a,19} organic PBUs, solid-state NMR studies on isotypical diamagnetic materials can provide fundamental data on both the composition of the asymmetric unit and phase purity of the bulk sample due to its high sensitivity. The ³¹P MAS spectrum shows the presence of three well-resolved isotropic resonances peaking at 15.3, 19.7 and 23.4 ppm (Fig. S9 in the ESI†). In addition, peak deconvolution and integration including the spinning sidebands yield a ratio of *ca.* 1.00 : 1.04 : 1.01 for these resonances. The ¹³C{¹H} CP MAS spectrum (Fig. S8 in the

ESI†) clearly shows two distinct spectral regions: the 29–41 ppm spectral range (peaks at 35.4 ppm and 36.8 ppm – shoulder) is attributed to the $-\text{CH}_2-$ groups, with its deficiency of spectral resolution being simultaneously attributed to very similar chemical environments (for the three expected groups) and to the likely existence of spin multiplets arising from ¹J_{C,P} coupling (usually in the 5–90 Hz range);²³ the aromatic carbon atoms from the ring appear instead in the 124–139 ppm window (peaks at 129.4, 130.1, 133.1 and 135.7 ppm). In summary, this bulk technique clearly supports the existence of a single crystallographically unique $\text{H}_3\text{bmt}^{3-}$ organic PBU in the asymmetric unit. Additionally, and based on the performed photoluminescence studies (see dedicated section), the material should also contain a single independent lanthanide center. These results are in perfect agreement with the performed crystallographic studies (see following section).

As also ascertained by powder X-ray diffraction studies (Fig. 1), vibrational FT-IR spectroscopy studies (Fig. S10 in the ESI†) clearly support the fact that bulk materials **1** to **6** are indeed isotypical. Fig. S10† shows the two most relevant regions of the spectra providing tentative assignments for the most diagnostic vibrational bands:²⁴ those present in the 3700–2500 cm^{-1} region arise mainly from stretching vibrations of O–H (from water molecules, both coordinated and of crystallization, and the PO–H groups) and $-\text{CH}_2-$ groups; between 400 and 1700 cm^{-1} the spectra are significantly more complex being dominated by the vibrational modes associated with coordinated phosphonate groups, aromatic ring vibrations and the in-plane deformation of water molecules (peaking around *ca.* 1600 cm^{-1}).

2.4. Crystal structure description and thermal behaviour

Thermogravimetry and thermodiffractionometry of $[\text{La}_2(\text{H}_3\text{bmt})_2(\text{H}_2\text{O})_2] \cdot \text{H}_2\text{O}$. Bulk $[\text{Ln}_2(\text{H}_3\text{bmt})_2(\text{H}_2\text{O})_2] \cdot \text{H}_2\text{O}$ materials [where $\text{Ln}^{3+} = \text{La}^{3+}$ (**1**), Ce^{3+} (**2**), Pr^{3+} (**3**), Nd^{3+} (**4**), $(\text{La}_{0.95}\text{Eu}_{0.05})^{3+}$ (**5**) and $(\text{La}_{0.95}\text{Tb}_{0.05})^{3+}$ (**6**)] exhibit a very similar thermal behaviour with increasing temperature as listed in the dedicated Materials and methods section (thermogram for **1** given in Fig. 2; thermograms for **2** to **6** are provided in Fig. S11 in the ESI†). In order to fully understand the structural modifications of the materials with temperature, thermodiffractionometry between ambient temperature and *ca.* 600 °C was performed for $[\text{La}_2(\text{H}_3\text{bmt})_2(\text{H}_2\text{O})_2] \cdot \text{H}_2\text{O}$ (**1**) (Fig. 2). We note that the results and conclusions described in the following paragraphs have been experimentally derived only for the La^{3+} -based material (**1**). It is, however, feasible to assume that all members of this series should behave in a very similar fashion as, for example, concluded from the photoluminescent studies on the mixed-lanthanide materials.

Between ambient temperature and *ca.* 265 °C, **1** releases a total of 4.9% of its weight in a clear two-step fashion (peaks at 69 and 162 °C). This loss agrees well with the release of the total amount of water molecules described by the empirical formula (for 3 water molecules a theoretical weight loss of *ca.* 5.2% is estimated). As found from the crystallographic studies (see below), the structures house a total of one disordered water molecule which is readily released in a very early stage: between ambient temperature and *ca.* 130 °C there is a continuous weight loss of 1.4% corresponding to the liberation of the solvent of crystallization (calculated as *ca.* 1.7%). As observed from the

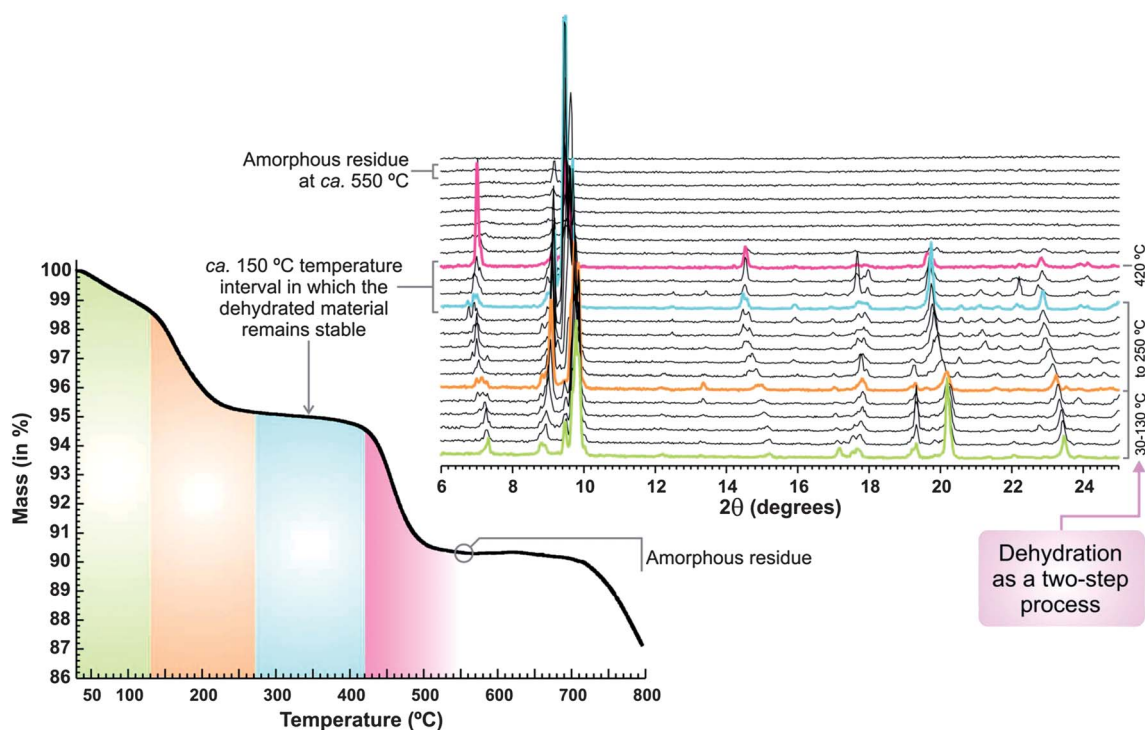


Fig. 2 Thermogram and variable temperature powder X-ray diffraction study of $[\text{La}_2(\text{H}_3\text{bmt})_2(\text{H}_2\text{O})_2]\cdot\text{H}_2\text{O}$ (**1**).

thermodiffraction studies, this release induces very small modifications in the crystal structure. The second stage of solvent liberation corresponds to those that are coordinated to the La^{3+} centers (see structural details below), occurring between *ca.* 130 and 265 °C (weight loss observed: 3.5%, calculated: 3.4%); above *ca.* 130 °C the powder X-ray diffraction patterns clearly show a progressive structural modification of the material up to the *in situ* formation of the completely dehydrated form, $[\text{La}(\text{H}_3\text{bmt})]$ (**1-dehyd**). This framework remains structurally stable over a temperature window of about 150 °C. At *ca.* 420 °C thermal decomposition (most probably due to oxidation of the organic component) settles in, leading to the formation of an amorphous residue (Fig. 2).

It is worth noting that the complete dehydration of **1** could be achieved by both increasing temperature (as described above) and also by placing the material under a high vacuum (as ascertained from the photoluminescence studies for the mixed-lanthanide material with Eu^{3+} – see Subsection 2.5). Moreover, the completely dehydrated materials could readily revert to their original form on exposure to air. We note that this typical zeolitic behaviour was tested *in situ* for a number of cycles with little or no loss of overall crystallinity being observed. This structural robustness was of crucial importance to isolate the completely dehydrated material and unveil its crystal structure by single-crystal X-ray diffraction studies (see below).

Crystal structure description of $[\text{La}_2(\text{H}_3\text{bmt})_2(\text{H}_2\text{O})_2]\cdot\text{H}_2\text{O}$ and $[\text{La}(\text{H}_3\text{bmt})]$. Large single-crystals of $[\text{Ln}_2(\text{H}_3\text{bmt})_2(\text{H}_2\text{O})_2]\cdot\text{H}_2\text{O}$ materials [where $\text{Ln}^{3+} = \text{La}^{3+}$ (**1**), Ce^{3+} (**2**), Pr^{3+} (**3**), and Nd^{3+} (**4**)] were directly harvested from the reaction vessels and their crystal structure was determined in the centrosymmetric monoclinic $C2/c$ space group using single-crystal X-ray diffraction

(Table 1). Phase identification and purity of the mixed-lanthanide materials **5** and **6** [where $\text{Ln}^{3+} = (\text{La}_{0.95}\text{Eu}_{0.05})^{3+}$ (**5**) and $(\text{La}_{0.95}\text{Tb}_{0.05})^{3+}$ (**6**)] were confirmed using powder X-ray diffraction, FT-IR spectroscopy and elemental analysis. The crystal structure of the dehydrated material of **1** ($[\text{La}(\text{H}_3\text{bmt})]$, **1-dehyd**) was also unequivocally unveiled from single-crystal X-ray diffraction. The structural details in the following paragraphs will be, therefore, solely based on the La^{3+} materials (as-prepared and dehydrated), and are assumed to be valid for the remaining members of the series.

The asymmetric units of **1** and **1-dehyd** are composed of a single crystallographically independent La^{3+} centre and one entire molecular unit of the deprotonated $\text{H}_3\text{bmt}^{3-}$ organic linker. These crystallographic details are in good agreement with the structural features derived from both the solid-state NMR studies (see above) and the detailed photoluminescence investigations (see following section). In **1**, the La^{3+} center is eight-coordinated, $\{\text{LaO}_8\}$, to a total of six phosphonate groups (from six symmetry-related $\text{H}_3\text{bmt}^{3-}$ anionic ligands) and one disordered water molecule (over two distinct locations – O1W and O2W – with 50% of rate of occupancy for each), with the overall coordination polyhedron resembling a highly distorted capped pentagonal bipyramid. The removal of the coordinated water molecule to yield **1-dehyd** (by heating above 100 °C with or without high vacuum) leads to a seven-coordinate environment, $\{\text{LaO}_7\}$, with the overall geometry now resembling a simple distorted pentagonal bipyramid (the capping position was occupied by the solvent molecule – see Fig. 3a and b). This seamless transformation is concomitantly accompanied by only small adjustments in the geometrical parameters of the coordination polyhedra, as clearly registered by the tabulated La–O distances and O–La–O angles presented in Tables 2 and 3,

Table 1 Crystal and structure refinement data for $[\text{Ln}_2(\text{H}_3\text{bmt})_2(\text{H}_2\text{O})_2] \cdot \text{H}_2\text{O}$ [where $\text{Ln}^{3+} = \text{La}^{3+}$ (1), Ce^{3+} (2), Pr^{3+} (3), and Nd^{3+} (4)], and the dehydrated form of material 1

	La^{3+} (1)	La^{3+} (1-dehyd)	Ce^{3+} (2)	Pr^{3+} (3)	Nd^{3+} (4)
Formula	$\text{C}_{18}\text{H}_{30}\text{La}_2\text{O}_{21}\text{P}_6$	$\text{C}_8\text{H}_{12}\text{LaO}_9\text{P}_3$	$\text{C}_{18}\text{H}_{30}\text{Ce}_2\text{O}_{21}\text{P}_6$	$\text{C}_{18}\text{H}_{30}\text{O}_{21}\text{Pr}_2$	$\text{C}_{18}\text{H}_{30}\text{Nd}_2\text{O}_{21}\text{P}_6$
Formula weight	1046.06	496.01	1048.48	1050.06	1056.72
Temperature/K	180(2)	150(2)	150(2)	150(2)	150(2)
Crystal system	Monoclinic	Monoclinic	Monoclinic	Monoclinic	Monoclinic
Space group	$C2/c$	$C2/c$	$C2/c$	$C2/c$	$C2/c$
$a/\text{\AA}$	23.5921(6)	24.757(4)	23.3599(13)	23.368(4)	23.419(5)
$b/\text{\AA}$	7.2774(2)	7.1588(13)	7.2198(4)	7.2040(11)	7.1793(16)
$c/\text{\AA}$	19.7125(5)	19.353(4)	19.7793(11)	19.745(3)	19.697(4)
$\beta/^\circ$	106.1760(10)	108.455(7)	106.034(2)	106.262(7)	106.650(14)
Volume/ \AA^3	3250.43(15)	3253.6(10)	3206.1(3)	3190.9(9)	3172.8(12)
Z	4	8	4	4	4
$D/\text{g cm}^{-3}$	2.138	2.025	2.172	2.186	2.212
$\mu(\text{Mo-K}\alpha)/\text{mm}$	2.974	2.959	3.190	3.406	3.627
$F(000)$	2040	1920	2048	2056	2064
Crystal size/mm	$0.12 \times 0.08 \times 0.04$	$0.11 \times 0.10 \times 0.07$	$0.08 \times 0.02 \times 0.01$	$0.08 \times 0.06 \times 0.04$	$0.07 \times 0.01 \times 0.01$
Crystal type	Colourless prisms	Colourless prisms	Colourless prisms	Colourless prisms	Colourless prisms
θ range	3.60 to 29.13	3.54 to 33.13	3.63 to 29.13	3.51 to 25.35	3.52 to 29.12
Index ranges	$-32 \leq h \leq 32,$ $-9 \leq k \leq 9,$ $-26 \leq l \leq 26$	$-38 \leq h \leq 38,$ $-10 \leq k \leq 11,$ $-29 \leq l \leq 29$	$-31 \leq h \leq 31,$ $-9 \leq k \leq 9,$ $-27 \leq l \leq 25$	$-27 \leq h \leq 28,$ $-8 \leq k \leq 6,$ $-23 \leq l \leq 23$	$-27 \leq h \leq 32,$ $-9 \leq k \leq 9,$ $-26 \leq l \leq 26$
Reflections collected	33 829	49 338	37 494	7961	18 869
Independent reflections	4356 ($R_{\text{int}} = 0.0408$)	6180 ($R_{\text{int}} = 0.0233$)	4291 ($R_{\text{int}} = 0.0410$)	2904 ($R_{\text{int}} = 0.0864$)	4251 ($R_{\text{int}} = 0.1118$)
Data completeness	$2\theta = 29.13^\circ,$ 99.8%	$2\theta = 33.13^\circ,$ 99.9%	$2\theta = 29.13^\circ,$ 99.4%	$2\theta = 25.35^\circ,$ 99.0%	$2\theta = 29.12^\circ,$ 99.6%
Final R indices	$R1 = 0.0226,$ $[I > 2\sigma(I)]^{a,b}$ $wR2 = 0.0501$	$R1 = 0.0208,$ $wR2 = 0.0510$	$R1 = 0.0226,$ $wR2 = 0.0462$	$R1 = 0.0497,$ $wR2 = 0.1043$	$R1 = 0.0466,$ $wR2 = 0.0703$
Final R indices (all data) ^{a,b}	$R1 = 0.0310,$ $wR2 = 0.0535$	$R1 = 0.0229,$ $wR2 = 0.0520$	$R1 = 0.0307,$ $wR2 = 0.0486$	$R1 = 0.0998,$ $wR2 = 0.1213$	$R1 = 0.0974,$ $wR2 = 0.0810$
Weighting scheme ^c	$m = 0.0229,$ $n = 6.7710$	$m = 0.0215,$ $n = 9.2013$	$m = 0.0189,$ $n = 7.2069$	$m = 0.0570,$ $n = 0$	$m = 0.0154,$ $n = 0$
Largest diff. peak and hole	0.690 and $-0.722 \text{ e}\text{\AA}^{-3}$	2.426 and $-0.887 \text{ e}\text{\AA}^{-3}$	0.486 and $-0.612 \text{ e}\text{\AA}^{-3}$	1.537 and $-1.756 \text{ e}\text{\AA}^{-3}$	1.036 and $-1.188 \text{ e}\text{\AA}^{-3}$
CCDC deposition number	846599	846598	846600	846601	846602

^a $R1 = \sum \|F_o\| - |F_c| / \sum \|F_o\|$. ^b $wR2 = \sqrt{\sum [w(F_o^2 - F_c^2)^2] / \sum [w(F_o^2)^2]}$. ^c $w = 1/[\sigma^2(F_o^2) + (mP)^2 + nP]$ where $P = (F_o^2 + 2F_c^2)/3$.

respectively. These small modifications are attributed to the intrinsic need to accommodate the extra coordinative position left vacant by the liberation of the coordinated solvent molecule. The La–O bond lengths are, therefore, found in the 2.3365(18)–2.6908(17) Å and 2.3293(14)–2.6459(12) Å ranges for **1** and **1-dehyd**, respectively. As expected, the reduction in the coordination number of La^{3+} also leads to an associated reduction of all bond lengths. It is further noted that the longest La–O bond lengths registered for both structures [2.6908(17) and 2.6029(16) Å for **1**; 2.6459(12) and 2.6012(12) Å for **1-dehyd** – see Table 2] are directly associated with the P2 phosphonate group which has a pivotal role in the structure architectures: besides being the sole phosphonate group which is *O,O*-chelated to La^{3+} (bite angles of 55.44(5) and 55.80(4)° for **1** and **1-dehyd**, respectively; see Fig. 3a and b), it further establishes physical connections between three adjacent metallic centres, leading to the formation of a one-dimensional zigzag lanthanum oxide chain running parallel to the [010] direction of the unit cell, assembled from edge-sharing of $\{\text{LaO}_8\}$ or $\{\text{LaO}_7\}$ polyhedra (Fig. 3c and d and 4).

The typical zeolitic-type behaviour observed for the $[\text{Ln}_2(\text{H}_3\text{bmt})_2(\text{H}_2\text{O})_2] \cdot \text{H}_2\text{O}$ materials concerning the water molecules can be rationalized taking solely into consideration the

observed structural features from the crystallographic studies. Both the coordinated and crystallization water molecules are located in hydrophilic cavities in the structure distributed in a parallel fashion to the aforementioned lanthanum oxide chains, which under high temperatures or high vacuum constitute an effective escape route for the solvent molecules (Fig. 3c–e). This process further leads to modifications in the lanthanum oxide chains. On the one hand, the observed intermetallic La...La distance is reduced by ca. 3% from 4.1984(2) Å to 4.0864(6) Å. On the other hand, the absence of the water molecules (coordinated and in the cavities), which are engaged in O–H...O hydrogen bonds with the neighbouring P1 phosphonate groups (Table 4), induces a modification of the hydrogen bonding network: the P1–O2–H2 moiety becomes free to rotate and establish a new interaction with the neighbouring *O,O*-chelated P2 phosphonate group (Fig. 4).

Topological studies of $[\text{La}_2(\text{H}_3\text{bmt})_2(\text{H}_2\text{O})_2] \cdot \text{H}_2\text{O}$ and $[\text{La}(\text{H}_3\text{bmt})]$. The structural complexity of the $[\text{Ln}_2(\text{H}_3\text{bmt})_2(\text{H}_2\text{O})_2] \cdot \text{H}_2\text{O}$ materials described in the previous subsection, in particular the high connectivity associated with the phosphonate groups, can be significantly reduced if the networks are treated mathematically by simplifying them into central

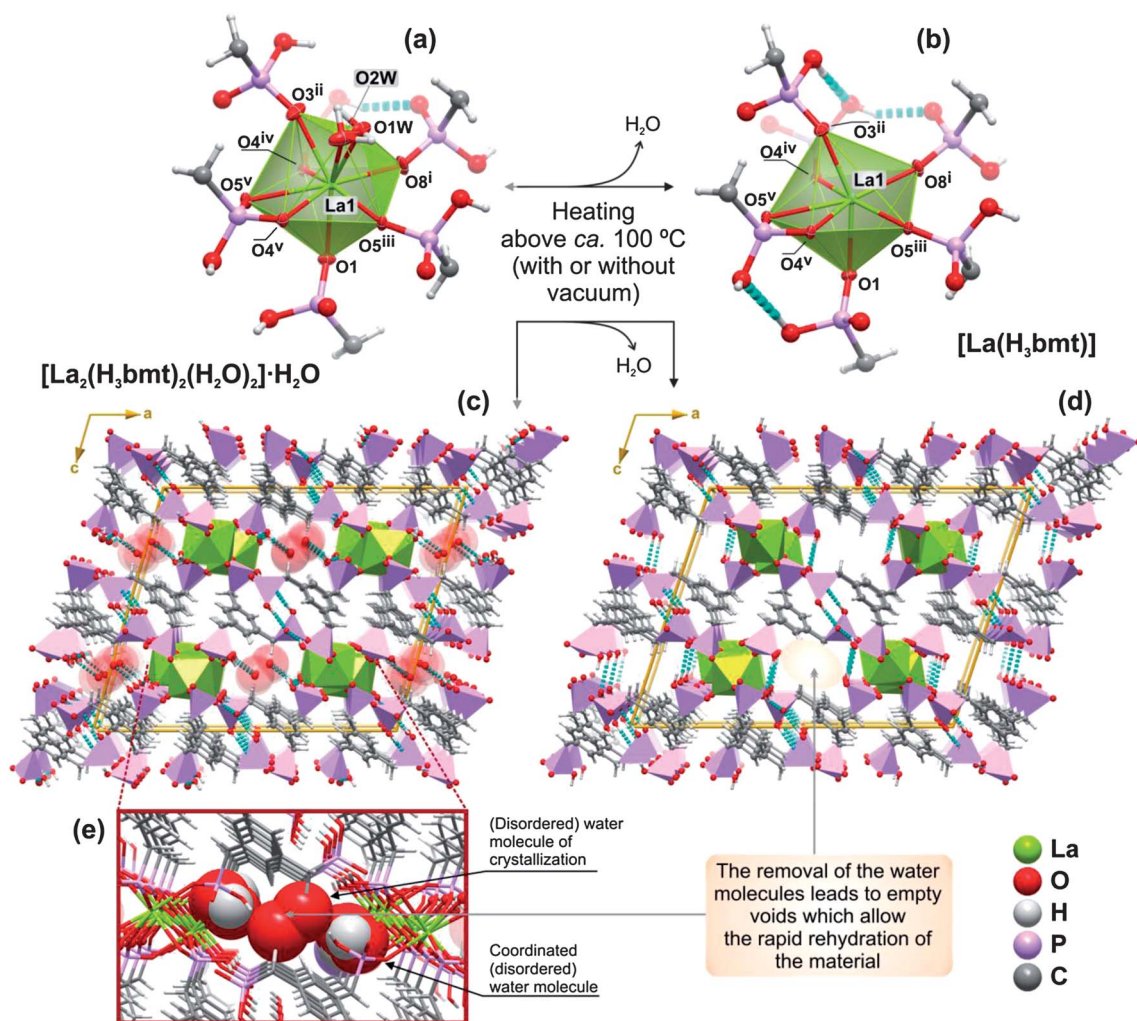


Fig. 3 Side by side comparison between the La^{3+} coordination environments and crystal packing features of $[\text{La}_2(\text{H}_3\text{bmt})_2(\text{H}_2\text{O})_2]\cdot\text{H}_2\text{O}$ (**1**) and $[\text{La}(\text{H}_3\text{bmt})]$ (**1-dehyd**). (a and b) Distorted $\{\text{LaO}_8\}$ and $\{\text{LaO}_7\}$ capped and simple pentagonal bipyramidal coordination environments present in compounds **1** and **1-dehyd**, respectively, emphasizing the location of the coordinated water molecule in the former material and the slight modifications in the local environment induced by its release. For selected bond lengths (in Å) and angles (in degrees) see Tables 2 and 3. Symmetry transformations used to generate equivalent atoms: (i) $-\frac{1}{2} + x, -\frac{1}{2} + y, z$; (ii) $\frac{1}{2} - x, -\frac{1}{2} + y, \frac{1}{2} - z$; (iii) $\frac{1}{2} - x, 2.5 - y, -z$; (iv) $\frac{1}{2} - x, 1.5 - y, -z$; (v) $x, 2 - y, \frac{1}{2} + z$. (c and d) Crystal packing of **1** and **1-dehyd** viewed in perspective along the $[010]$ direction of the unit cell. The disordered water molecules of crystallization and those coordinated to the La^{3+} in **1** are depicted in space-filling mode (zoom perspective in (e)) so as to better illustrate the presence of framework apertures which facilitate the removal of these moieties upon heating of the material. Hydrogen bonding interactions are shown as dashed dark green lines. For details on the geometry of the represented $\text{O}-\text{H}\cdots\text{O}$ interactions see Table 4.

Table 2 Bond lengths (in Å) for the La^{3+} coordination environments present in $[\text{La}_2(\text{H}_3\text{bmt})_2(\text{H}_2\text{O})_2]\cdot\text{H}_2\text{O}$ (**1**) and $[\text{La}(\text{H}_3\text{bmt})]$ (**1-dehyd**)^a

	La^{3+} (1)	La^{3+} (1-dehyd)
La1–O1	2.4660(19)	2.3933(14)
La1–O3 ⁱⁱ	2.417(2)	2.3720(14)
La1–O4 ^{iv}	2.5628(17)	2.4863(13)
La1–O4 ^v	2.6908(17)	2.6459(12)
La1–O5 ⁱⁱⁱ	2.4990(18)	2.4555(13)
La1–O5 ^v	2.6029(16)	2.6012(12)
La1–O8 ⁱ	2.3365(18)	2.3293(14)
La1–O1W	2.559(6)	—
La1–O2W	2.617(6)	—

^a Symmetry transformations used to generate equivalent atoms: (i) $-\frac{1}{2} + x, -\frac{1}{2} + y, z$; (ii) $\frac{1}{2} - x, -\frac{1}{2} + y, \frac{1}{2} - z$; (iii) $\frac{1}{2} - x, 2.5 - y, -z$; (iv) $\frac{1}{2} - x, 1.5 - y, -z$; (v) $x, 2 - y, \frac{1}{2} + z$.

nodes and connecting rods (*i.e.*, bridges between the selected nodes).^{2a,25} Topological studies have been performed using the software package TOPOS.²⁶

As described in the previous section, the $[\text{Ln}_2(\text{H}_3\text{bmt})_2(\text{H}_2\text{O})_2]\cdot\text{H}_2\text{O}$ materials, in particular the La^{3+} -based material, exhibit a typical zeolitic behaviour concerning the solvent molecules. The reversible dehydration–rehydration is not accompanied by the modification of the local connectivity associated with the phosphonate groups. Therefore, both $[\text{La}_2(\text{H}_3\text{bmt})_2(\text{H}_2\text{O})_2]\cdot\text{H}_2\text{O}$ (**1**) and $[\text{La}(\text{H}_3\text{bmt})]$ (**1-dehyd**) share the same topology, this being another structural factor which helps in explaining the observed zeolitic properties. Each crystallographically independent metallic center (La^{3+}) was taken as a network node, with the intermetallic bridges being ensured by the bridging ligands. Because the tripodal $\text{H}_3\text{bmt}^{3-}$ linker

Table 3 Bond angles (in degrees) for the La³⁺ coordination environments present in [La₂(H₃bmt)₂(H₂O)₂]·H₂O (**1**) and [La(H₃bmt)] (**1-dehyd**)^a

	1	1-dehyd		1
O1–La1–O4 ^{iv}	76.16(6)	86.57(5)	O1–La1–O1W	151.44(13)
O1–La1–O4 ^v	84.29(6)	84.64(5)	O1–La1–O2W	145.38(14)
O1–La1–O5 ⁱⁱⁱ	82.18(6)	84.59(5)	O3 ⁱⁱ –La1–O1W	63.09(14)
O1–La1–O5 ^v	75.44(6)	77.62(5)	O3 ⁱⁱ –La1–O2W	62.82(15)
O3 ⁱⁱ –La1–O1	144.45(7)	156.00(5)	O4 ^{iv} –La1–O2W	137.62(14)
O3 ⁱⁱ –La1–O4 ^{iv}	75.90(6)	81.81(5)	O5 ⁱⁱⁱ –La1–O1W	69.26(13)
O3 ⁱⁱ –La1–O4 ^v	94.57(7)	85.68(5)	O5 ⁱⁱⁱ –La1–O2W	68.09(15)
O3 ⁱⁱ –La1–O5 ⁱⁱⁱ	130.84(6)	112.73(5)	O5 ^v –La1–O2W	105.32(16)
O3 ⁱⁱ –La1–O5 ^v	74.86(7)	78.77(5)	O8 ⁱ –La1–O1W	77.46(13)
O4 ^{iv} –La1–O4 ^v	125.71(4)	126.91(3)	O8 ⁱ –La1–O2W	93.70(16)
O4 ^{iv} –La1–O5 ^v	70.64(5)	71.16(4)	O1W–La1–O4 ^{iv}	130.36(13)
O5 ⁱⁱⁱ –La1–O4 ^{iv}	150.85(6)	159.24(4)	O1W–La1–O4 ^v	85.94(12)
O5 ⁱⁱⁱ –La1–O4 ^v	70.16(5)	70.87(4)	O1W–La1–O5 ^v	119.67(13)
O5 ^v –La1–O4 ^v	55.44(5)	55.80(4)	O1W–La1–O2W	16.83(15)
O5 ⁱⁱⁱ –La1–O5 ^v	122.36(4)	124.73(3)	O2W–La1–O4 ^v	69.53(14)
O8 ⁱ –La1–O1	97.23(7)	106.74(5)		
O8 ⁱ –La1–O3 ⁱⁱ	101.99(8)	93.65(6)		
O8 ⁱ –La1–O4 ^{iv}	85.42(6)	87.29(5)		
O8 ⁱ –La1–O4 ^v	147.77(6)	145.09(5)		
O8 ⁱ –La1–O5 ⁱⁱⁱ	78.13(6)	77.37(5)		
O8 ⁱ –La1–O5 ^v	155.97(6)	157.89(4)		

^a Symmetry transformations used to generate equivalent atoms: (i) $-\frac{1}{2} + x, -\frac{1}{2} + y, z$; (ii) $\frac{1}{2} - x, -\frac{1}{2} + y, \frac{1}{2} - z$; (iii) $\frac{1}{2} - x, 2.5 - y, -z$; (iv) $\frac{1}{2} - x, 1.5 - y, -z$; (v) $x, 2 - y, \frac{1}{2} + z$.

connects to more than two metallic centers (μ_n),^{2b} its center of gravity was also taken as a network node (Fig. 5, right bottom corner). The [Ln₂(H₃bmt)₂(H₂O)₂]·H₂O materials and their dehydrated forms (exemplified in Fig. 5 for **1** and **1-dehyd**) are, thus, binodal 6,6-connected networks with an overall Schafli symbol of {4¹⁰.6⁵} {4¹¹.6⁴}. Searches in the *Reticular Chemistry Structure Resource* (RCSR)²⁷ and in EPINET²⁸ reveal that this nodal connectivity is, to the best of our knowledge, unprecedented among MOF structures.

2.5. Photoluminescence

The inclusion of optically active lanthanide centers (such as Eu³⁺ and Tb³⁺) into the La³⁺ matrix of compound **1** leads to the formation of new materials capable of converting UV radiation into visible light at room temperature as shown in Fig. 6 for [(La_{0.95}Eu_{0.05})₂(H₃bmt)₂(H₂O)₂]·H₂O (**5**) and [(La_{0.95}Tb_{0.05})₂(H₃bmt)₂(H₂O)₂]·H₂O (**6**). The excitation and emission spectra, and the ⁵D₄ decay curves of **6** and its dehydrated form, [(La_{0.95}Tb_{0.05})(H₃bmt)] (**6-dehyd**), are provided as ESI.† In the following paragraphs we shall focus our discussion only on the Eu³⁺-containing compounds. We also briefly discuss the photoluminescence properties of the compound [La₂(H₃bmt)₂(H₂O)₂]·H₂O (**1**), which are characteristic of its organic PBUs and can only be discerned at low temperatures.

The excitation spectrum of [(La_{0.95}Eu_{0.05})₂(H₃bmt)₂(H₂O)₂]·H₂O (**5**) was recorded at 298 and 11 K while monitoring within the Eu³⁺ ⁵D₀ → ⁷F₂ transition (Fig. 7a). Both spectra are dominated by two broad UV bands (240–288 and 288–340 nm) which may be attributed to π–π* transitions of the organic PBUs. This attribution was confirmed by recording at 11 K the excitation spectrum of **1** while monitoring the phosphorescence emission at 445 nm (Fig. 7a). The sharp lines are assigned to the ⁷F_{0,1} → ⁵D_{1–4}, ⁵L₆, ⁵G_{2–6}, ⁵H_{3–7} and ⁵F_{1–5} Eu³⁺ intra-4f⁶ transitions. A similar band assignment of the excitation spectra can

be performed for the fully dehydrated form of **5**, [(La_{0.95}Eu_{0.05})(H₃bmt)] (**5-dehyd**) (Fig. 7b), prepared *in situ* by the dehydration of **5** at *ca.* 450 K and under a high vacuum (*ca.* 5 × 10^{−6} mbar). For this latter material the intensity of the UV broad bands are significantly more distinct and the Eu³⁺ intra-4f⁶ transitions are more noticeable, in particular the ⁷F₀ → ⁵D₀ transition which is almost absent in **5**.

The emission spectra of **5** and **5-dehyd** recorded at 298 and 11 K (excited at 393 nm) are provided in Fig. 8a and b, respectively. The sharp lines are assigned to transitions between the first excited non-degenerate ⁵D₀ state and the ⁷F_{0–4} levels of the fundamental Eu³⁺ septet. Except for ⁵D₀ → ⁷F₁, which has a predominant magnetic-dipole character independent of the Eu³⁺ crystal site, the observed transitions are mainly of electric-dipole nature. The presence of one single line for the ⁵D₀ → ⁷F₀ transition and the local-field splitting of the ⁷F_{1,2} levels into three and a maximum of five Stark components, respectively, and the predominance of the ⁵D₀ → ⁷F₂ transition relative to the ⁵D₀ → ⁷F₁ indicates the presence of a single low-symmetry Eu³⁺ environment without inversion symmetry in both structures, as supported by the crystal structure determination (see dedicated section for details). Eu³⁺ emission is highly sensitive to small modifications on the first coordination sphere of the metal, such as the variation of the number and type of coordinated moieties. Thus, the reversible transformation of **5** into **5-dehyd**, due to the release and subsequent absorption of water molecules, can easily be accompanied by photoluminescence (Fig. 8c and d). Under the employed experimental conditions (high vacuum), the structural change on the first coordination sphere of Eu³⁺ starts at *ca.* 350 K and is nearly complete at 400 K (Fig. 8c). The starting form can be regenerated with subsequent exposure of the dehydrated material to air under normal ambient conditions (Fig. 8d). We note that these temperatures are slightly distinct from, but still very comparable to, those observed both in the TGA measurements and in the thermodiffraction studies. We

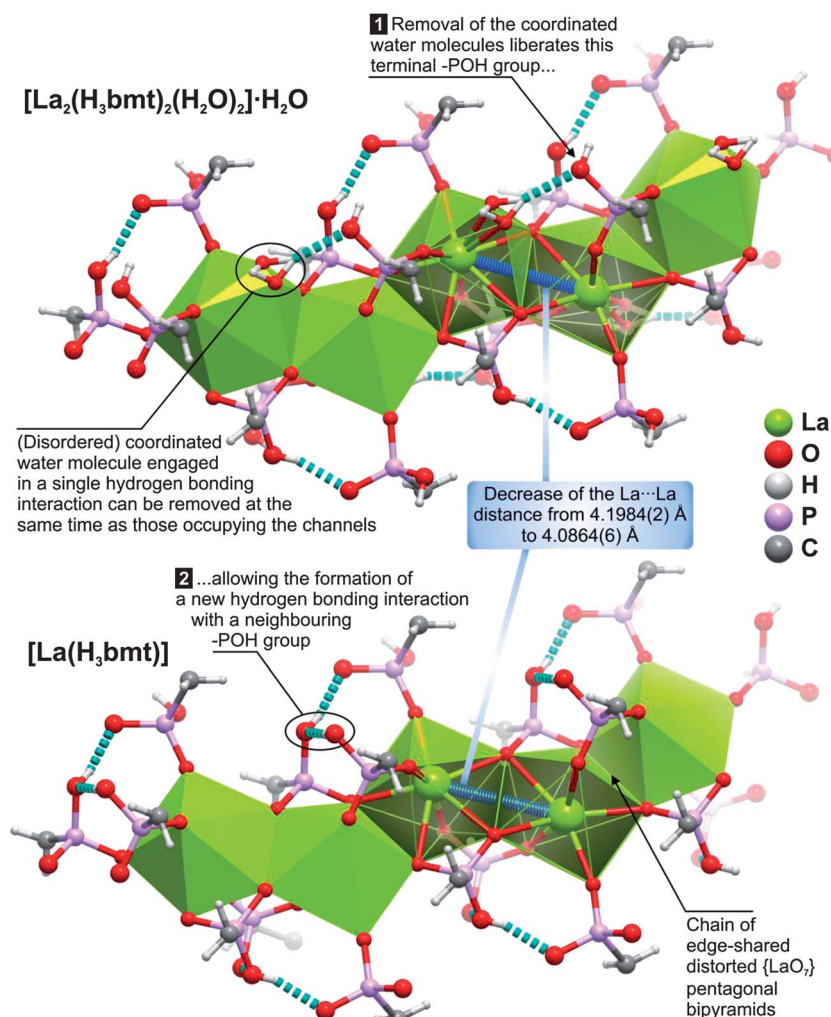


Fig. 4 Fragments of the crystal structures of $[\text{La}_2(\text{H}_3\text{bmt})_2(\text{H}_2\text{O})_2] \cdot \text{H}_2\text{O}$ (**1**) and $[\text{La}(\text{H}_3\text{bmt})]$ (**1-dehyd**) showing the lanthanum oxide chains formed by the edge-sharing of either $\{\text{LaO}_8\}$ or $\{\text{LaO}_7\}$ polyhedra. The representation depicts how the release of the coordinated water molecules in **1** affects the hydrogen bonding network present in the crystal structures and the inter-lanthanide distance across the zigzag chains.

attribute the small differences to the fact that the photoluminescence studies have been performed under vacuum, which greatly facilitates the release of all water molecules. Dehydration

Table 4 Geometrical details (distances in Å and angles in degrees) of the hydrogen bonds present in $[\text{La}_2(\text{H}_3\text{bmt})_2(\text{H}_2\text{O})_2] \cdot \text{H}_2\text{O}$ (**1**) and $[\text{La}(\text{H}_3\text{bmt})]$ (**1-dehyd**)^a

D-H...A	<i>d</i> (D...A)	<(DHA)
1		
O1W-H2X...O2 ^{vi}	2.866(6)	158
O2W-H1X...O2 ^{vi}	2.800(7)	147
O2-H2...O3W	2.559(5)	155
O2-H2...O3W ^{vii}	3.136(6)	128
O6-H6...O9 ^{viii}	2.571(3)	158
O7-H7...O9 ^{viii}	2.594(3)	169
1-dehyd		
O2-H2...O6 ^{ix}	2.815(2)	177
O6-H6...O9 ^{viii}	2.4906(18)	155
O7-H7...O9 ^{viii}	2.5903(19)	168

^a Symmetry transformations used to generate equivalent atoms: (vi) $\frac{1}{2} - x, \frac{1}{2} + y, \frac{1}{2} - z$; (vii) $1 - x, y, \frac{1}{2} - z$; (viii) $1 - x, 2 - y, -z$; (ix) $x, 2 - y, \frac{1}{2} + z$.

of **5** is accompanied by a boost in the emission efficiency of the material with a *ca.* 1.7 fold increase in the integrated emission intensity (Fig. 8d). The ratio between the integrated intensities of the $^5\text{D}_0 \rightarrow ^7\text{F}_2$ and $^5\text{D}_0 \rightarrow ^7\text{F}_1$ transitions, $I(^5\text{D}_0 \rightarrow ^7\text{F}_2)/I(^5\text{D}_0 \rightarrow ^7\text{F}_1)$, known as the asymmetric ratio, was calculated as *ca.* 2.5 and 4.0 for **5** and **5-dehyd**, respectively. These values point to a slightly more distorted environment of the Eu^{3+} coordination polyhedron in the dehydrated material (please note: a low value indicates a lower distortion of local environment for Eu^{3+} , approaching the ideal case of an inversion center). This result agrees well with the performed crystallographic studies: while the release of the coordinated water molecule does not imply a considerable rearrangement of the coordination polyhedron of Eu^{3+} , it indeed leads to a more asymmetric environment as the bond angles to the apical positions of the pentagonal bipyramid become larger than those between the equatorially connected atoms.

The ambient temperature (298 K) $^5\text{D}_0$ lifetime of Eu^{3+} of **5** and **5-dehyd** was determined by monitoring the emission decay curves within the maximum of the $^5\text{D}_0 \rightarrow ^7\text{F}_2$ transition, using an excitation at *ca.* 393 nm (Fig. S12 in the ESI[†]). The decay curves

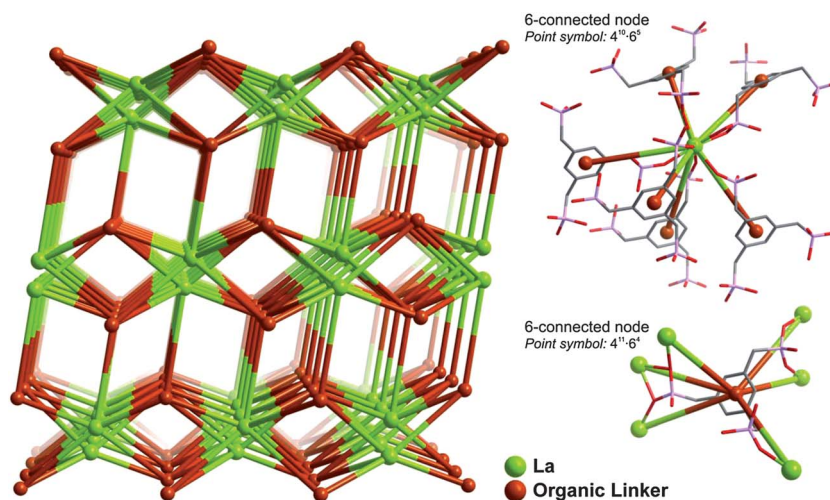


Fig. 5 Topological representation of the networks of $[\text{La}_2(\text{H}_3\text{bmt})_2(\text{H}_2\text{O})_2] \cdot \text{H}_2\text{O}$ (**1**) and $[\text{La}(\text{H}_3\text{bmt})]$ (**1-dehyd**). On the right side there is a representation of the individual connectivities of each of the nodes of the network: both the crystallographically independent La^{3+} center and the organic linker (the center of gravity of the aromatic ring was considered as the node) are connected to six adjacent nodes.

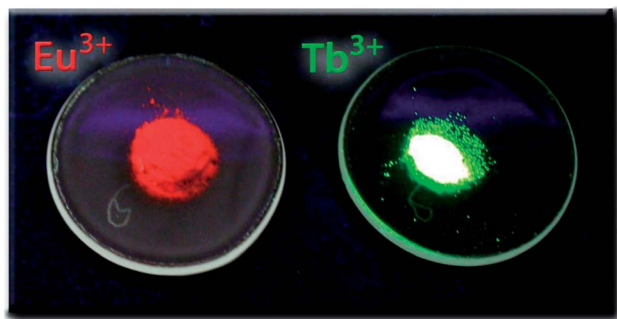


Fig. 6 Visible emission of the $[(\text{La}_{0.95}\text{Eu}_{0.05})_2(\text{H}_3\text{bmt})_2(\text{H}_2\text{O})_2] \cdot \text{H}_2\text{O}$ (**5**) and $[(\text{La}_{0.95}\text{Tb}_{0.05})_2(\text{H}_3\text{bmt})_2(\text{H}_2\text{O})_2] \cdot \text{H}_2\text{O}$ (**6**) materials when irradiated using a laboratory UV lamp ($\lambda = 254 \text{ nm}$).

were fitted by single exponential functions, yielding lifetimes of 0.60 ± 0.01 and 1.60 ± 0.01 ms for **5** and **5-dehyd**, respectively. This indicates the presence of a unique Eu^{3+} crystallographic site and clearly demonstrates the improvement of the decay time (*ca.* 2.7 times) with the removal of the coordinated water molecules due to the suppression of emission quenching through the coupling of the Eu^{3+} excited states with the vibrational states of the O–H oscillators.

Compounds **6** and **6-dehyd** (Fig. S13 in the ESI†) have similar excitation spectra at ambient temperature (298 K), being dominated by the broad UV band ranging from 240 to 288 nm and attributed to the ligand excited states. The Tb^{3+} intra- $4f^8$ transitions can be readily visualized after a magnification of the spectra. The enhancement of the broad UV band on the Tb^{3+} -containing compounds when compared with the Eu^{3+} -based materials may be explained by a more efficient energy transfer from the ligands to the Tb^{3+} cations, promoted by the superposition with the interconfigurational $4f^75d^1$ excited states of Tb^{3+} in this region of the spectrum.²⁹ The impact of the dehydration process of **6** into **6-dehyd** has also been studied: although in a smaller magnitude with respect to measurable effects, the emission spectra and $^5\text{D}_4$ decay curves recorded at 298 K

(Fig. S14 and S15 in the ESI†) yield comparable results to those discussed above for **5** and **5-dehyd**.

For reference, the complex photoluminescence properties of **1** are briefly given as ESI to this manuscript (Fig. S16 and S17†). At ambient temperature **1** emits only UV light, with a broad band peaking at 292 nm attributable to the $\text{S}_1 \rightarrow \text{S}_0$ transition arising from the organic PBU. Additionally a broad band peaking at 405 nm (12 K) appears with the decrease of temperature, presumably originating from the $\text{T}_1 \rightarrow \text{S}_0$ transition. Time-resolved and lifetime measurements recorded at 12 K (Fig. S16 and S17 in the ESI†) clearly demonstrate the fluorescent and phosphorescent nature of the 292 and 405 nm emission bands, respectively. We note that additional studies are required to fully understand the extra excitation broad bands at *ca.* 300 nm and their corresponding emission bands peaking at 410 and 435 nm (Fig. S16 in the ESI†).

Based on the emission spectra, $^5\text{D}_0$ lifetimes and empirical radiative and non-radiative transition rates, and assuming that only non-radiative and radiative processes are involved in the depopulation of the $^5\text{D}_0$ state, the $^5\text{D}_0$ quantum efficiency, q ,³⁰ has been determined for **5** and **5-dehyd**. The theoretical rationale employed in these calculations is provided as ESI.† The number of water molecules (n_w) coordinated to Eu^{3+} and Tb^{3+} may be determined using the empirical formula of Kimura and Kato (provided in the ESI†),³¹ also in agreement with the formula of Horrocks.³² Data, including the absolute emission quantum yield (measured experimentally), are displayed in Table 5 for compounds **5**, **5-dehyd** and **6**.

As expected, **5-dehyd** has a relatively high quantum efficiency (54%) when compared to the as-prepared material (15%). This occurs because of a relatively low non-radiative transition rate promoted by the suppression of the O–H oscillators associated with the coordinated water molecules, and the concomitant increment of the radiative transition rate. The measured maximum absolute emission quantum yield of **5** (4% at 280 nm) is, nevertheless, far from the calculated quantum efficiency indicating that part of the light absorbed into the ligand excited levels relaxes non-radiatively and does not reach the $^5\text{D}_0$ emitting

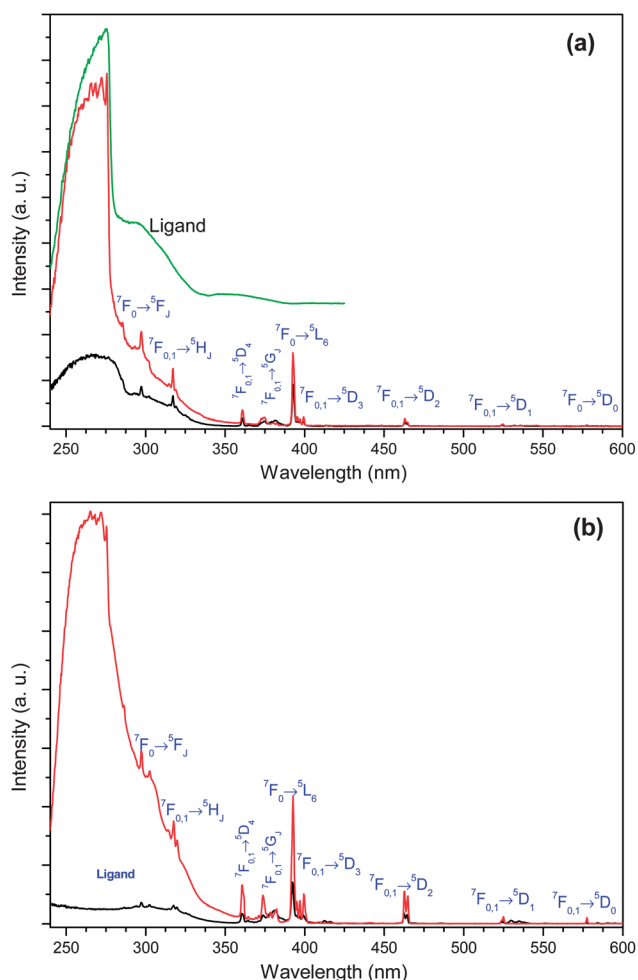


Fig. 7 (a) Excitation spectrum of $[\text{La}_2(\text{H}_3\text{bmt})_2(\text{H}_2\text{O})_2]\cdot\text{H}_2\text{O}$ (**1**) at 11 K (green line) while monitoring the emission at 445 nm, and excitation spectra of $[(\text{La}_{0.95}\text{Eu}_{0.05})_2(\text{H}_3\text{bmt})_2(\text{H}_2\text{O})_2]\cdot\text{H}_2\text{O}$ (**5**) at 298 (black line) and 11 K (red line) while monitoring the Eu^{3+} emission at 611.4 nm. (b) Excitation spectra of $[(\text{La}_{0.95}\text{Eu}_{0.05})(\text{H}_3\text{bmt})]$ (**5-dehyd**) at 298 (black line) and 11 K (red line) while monitoring the emission at 612.2 nm.

state. In contrast, compound **6** reaches a relatively high absolute emission quantum yield (46% at 280 nm excitation). Because of the large energy difference between the emitting levels of Eu^{3+} ($^5\text{D}_0$, 578 nm/17 300 cm^{-1}) and Tb^{3+} ($^5\text{D}_4$, 485 nm/20 620 cm^{-1}) and the zero-phonon triplet state energy level of the ligands (estimated at 358 nm/27 930 cm^{-1} from Fig. S16 in the ESI[†]), the energy transfer from the organic PBUs to the Eu^{3+} and Tb^{3+} does not occur directly to the emitter states, $^5\text{D}_0$ and $^5\text{D}_4$, respectively, but for high-energy levels. The high absolute emission quantum yield observed for **6** must then be interpreted by a good balance between absorption, energy transfer and emission rates. Note that, as the dehydrated materials readily rehydrate at normal ambient conditions it was not possible to measure their corresponding absolute emission quantum yields.

2.6. Heterogeneous catalysis

The catalytic performance of $[\text{La}_2(\text{H}_3\text{bmt})_2(\text{H}_2\text{O})_2]\cdot\text{H}_2\text{O}$ (**1**) was investigated in the ring-opening reaction of styrene oxide

(PhEtO) with methanol at 55 °C (Scheme 3). The only reaction product was 2-methoxy-2-phenylethanol (MeOPhEtOH), which was formed in 80% yield after 24 h of reaction. It is noteworthy that in the absence of the heterogeneous catalyst (but under similar reaction conditions) the conversion at 24 h was only *ca.* 10%. These results clearly show that **1** exhibits catalytic activity and excellent regioselectivity in the methanolysis of PhEtO to the β -alkoxy alcohol product. We note that high conversions were also reported for Cu- and Fe-based MOFs while using shorter reaction times and lower temperatures, but lower selectivities to the β -alkoxy alcohol were also observed (>93%).^{8a,33}

For comparative purposes the PBUs (organic linker and the lanthanide precursor) were also tested under similar reaction conditions as (homogeneous) catalysts (using amounts equivalent to those in the loaded MOF catalyst) in the methanolysis of PhEtO. In the case of the ligand (H_6bmt), MeOPhEtOH was formed in quantitative yields within 1 h of reaction, indicating that the organic PBU is a highly active and selective homogeneous Brønsted acid organocatalyst (Table 6), in agreement with the data reported for other related systems.³⁴ When the lanthanide precursor ($\text{LaCl}_3\cdot 7\text{H}_2\text{O}$) was employed as the catalyst, MeOPhEtOH was produced in 71% yield at 24 h reaction (93% selectivity). Comparably good results have also been reported for related systems³⁵ and also in the cases of ring opening of epoxides by CeCl_3 into β -halohydrins and β -haloamines.³⁶

The recyclability of the catalyst **1** was investigated for three consecutive batch runs in the reaction of PhEtO with methanol at 55 °C. Prior to reuse, the solid catalyst was separated from the reaction mixture by centrifugation, washed with *n*-hexane and dried overnight at ambient temperature. In all runs MeOPhEtOH was always the only reaction product and no decrease in catalytic activity was observed (Fig. 9). On the contrary we have observed an increase in the reaction rate from the first to the subsequent runs, most likely due to an increase in the number of effective active sites. Structural integrity of the catalyst after the first and the third runs was investigated using powder X-ray diffraction and electron microscopy (Fig. 10). These studies clearly show that despite the large crystals of the as-prepared catalyst **1** being fragmented during the catalytic process (which may result in an enhanced amount of effective active sites) leading to a small loss of overall crystallinity, the framework of the material remained intact.

In order to get a better insight into the hetero/homogeneous nature of the catalytic reaction a leaching test was performed for **1** which consisted in filtering the used catalyst (through a 0.20 μm nylon GVS membrane) after 4 h reaction, at 55 °C, and leaving the reaction solution under magnetic stirring for further 20 h. The ratio of the increments in conversion in the period of time of 4–24 h of the leaching test to those for the reaction without a catalyst is equal to 1, indicating that the catalytic reaction is heterogeneous in nature.

3. Concluding remarks

In this manuscript we have successfully described the preparation of an isotypical series of functional materials, formulated as $[\text{Ln}_2(\text{H}_3\text{bmt})_2(\text{H}_2\text{O})_2]\cdot\text{H}_2\text{O}$ [where $\text{Ln}^{3+} = \text{La}^{3+}$ (**1**), Ce^{3+} (**2**), Pr^{3+} (**3**), Nd^{3+} (**4**), $(\text{La}_{0.95}\text{Eu}_{0.05})^{3+}$ (**5**) and $(\text{La}_{0.95}\text{Tb}_{0.05})^{3+}$ (**6**)], all isolated as phase-pure large single crystals. The structural

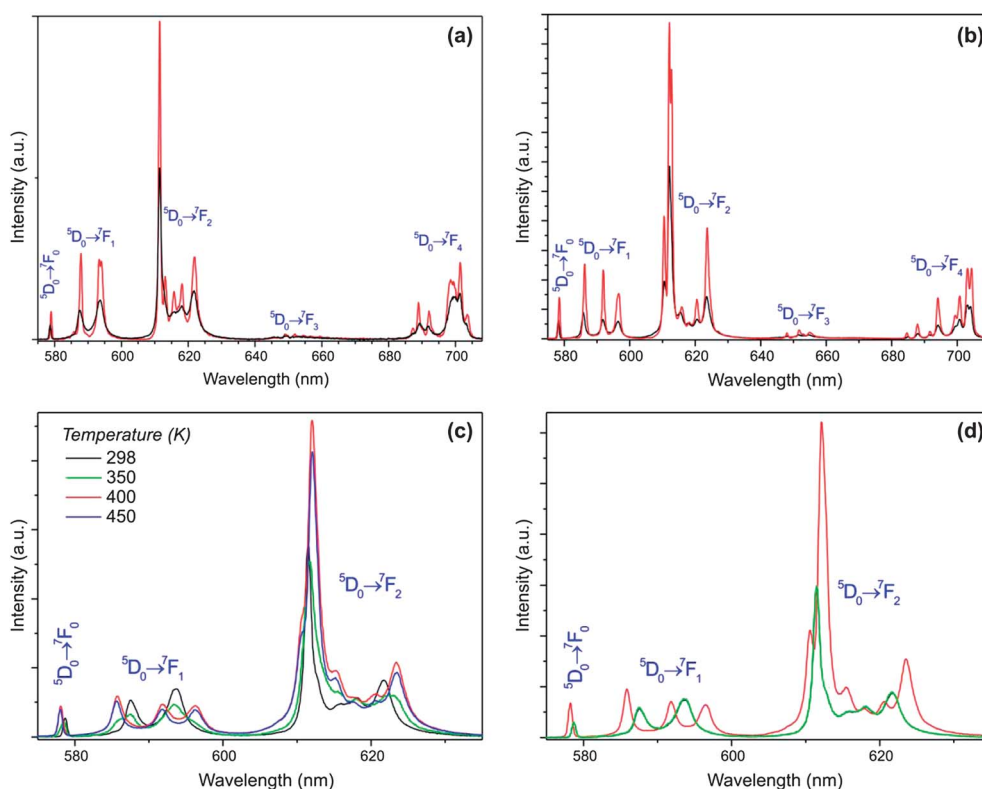


Fig. 8 (a and b) Emission spectra of $[(\text{La}_{0.95}\text{Eu}_{0.05})_2(\text{H}_3\text{bmt})_2(\text{H}_2\text{O})_2] \cdot \text{H}_2\text{O}$ (**5**) and $[(\text{La}_{0.95}\text{Eu}_{0.05})(\text{H}_3\text{bmt})]$ (**5-dehyd**), respectively, at 298 (black line) and 11 K (red line). (c) Partial emission spectra of **5** as a function of temperature and vacuum ($\lambda_{\text{exc}} = 393$ nm): the spectrum at 298 K was recorded at ambient pressure (1 bar) and the spectra at 350, 400 and 450 K were recorded under a vacuum of $\text{ca. } 5 \times 10^{-6}$ mbar. (d) Partial emission spectra of **5** and **5-dehyd** with $\lambda_{\text{exc}} = 393$ nm (ambient temperature: 298 K): black line, **5** at ambient pressure; red line, **5** after dehydration at 450 K under a vacuum of 5×10^{-6} mbar; and green line, after dehydration at 450 K followed by rehydration over a period of one day at ambient conditions (temperature and pressure). Please note: the green and black lines are nearly perfectly overlapped.

features and properties of all these materials have been thoroughly characterized in the solid-state using X-ray diffraction (both powder and single-crystal), FT-IR spectroscopy, thermogravimetry, electron microscopy (SEM and EDS), elemental analysis and solid-state NMR. Materials were found to exhibit dual functionality, namely photoluminescence (in particular the Tb^{3+} material) and catalytic activity.

Based on our previous studies using flexible tripodal polyphosphonate molecules, (benzene-1,3,5-triyltris(methylene)triphosphonic acid (H_6bmt) was carefully designed and selected to simultaneously promote structural robustness and effectively sensitize the lanthanide cations in order to boost the photoluminescent properties. Even though the synthesis of H_6bmt has

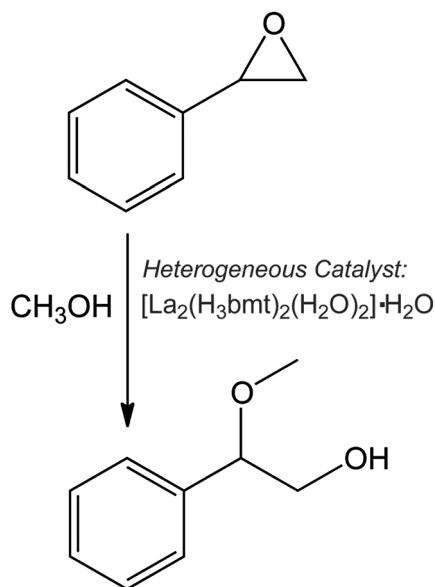
been previously reported in the literature, we have optimized a new two-step synthesis based on a Michaelis–Arbusov reaction of 1,3,5-tris(bromomethyl)benzene with triethyl phosphite. This method allows: (i) the isolation of large amounts of the desired linker, in (ii) short reaction times and (iii) in high yield and purity. The final tripodal linker (and its intermediate form) was fully characterized in the liquid state. The characterization data provided in the present manuscript complement the up to date available literature data.

Hydrothermal synthesis was found to be the most efficient synthetic route for the isolation of all the $[\text{Ln}_2(\text{H}_3\text{bmt})_2(\text{H}_2\text{O})_2] \cdot \text{H}_2\text{O}$ members in large amounts, large crystals and as phase-pure materials. It was discovered that temperatures as low as 100°C

Table 5 Experimental $^5\text{D}_0$ lifetime, τ ; radiative, k_r , and non-radiative, k_{nr} , transition rates; $^5\text{D}_0$ quantum efficiency, q ; absolute emission quantum yield, η ; and the estimated number of water molecules, n_w , for $[(\text{La}_{0.95}\text{Eu}_{0.05})_2(\text{H}_3\text{bmt})_2(\text{H}_2\text{O})_2] \cdot \text{H}_2\text{O}$ (**5**) and $[(\text{La}_{0.95}\text{Eu}_{0.05})(\text{H}_3\text{bmt})]$ (**5-dehyd**). The experimental $^5\text{D}_4$ lifetime, τ ; absolute emission quantum yield, η ; and the estimated number of water molecules, n_w , are also given for $[(\text{La}_{0.95}\text{Tb}_{0.05})_2(\text{H}_3\text{bmt})_2(\text{H}_2\text{O})_2] \cdot \text{H}_2\text{O}$ (**6**). Data have been obtained at ambient temperature (298 K)

Compound	τ [ms]	k_r [s^{-1}]	k_{nr} [s^{-1}]	q [%]	η [%] (λ_{exc} ; nm)	n_w^a
5	0.60 ± 0.01	248	1418	15	4 (280)/1 (393)	1.1
5-dehyd	1.60 ± 0.01	337	288	54	—	0
6	1.63 ± 0.01	—	—	—	46 (280)/3 (376)	1.4

^a Values calculated following the studies of Kimura and Kato.³¹ From the Horrocks' formula we obtain similar values for **5** and **5-dehyd** (1.23 and -0.02 , respectively).³²



Scheme 3 Reaction of styrene oxide with methanol, in the presence of the heterogeneous catalyst $[\text{La}_2(\text{H}_3\text{bmt})_2(\text{H}_2\text{O})_2] \cdot \text{H}_2\text{O}$ (**1**), to produce 2-methoxy-2-phenylethanol.

Table 6 Ring-opening reaction of styrene oxide with methanol at 55 °C^a

Catalyst	Reaction time (h)	Conversion ^b (%)	Selectivity ^c (%)
None	24	10	100
H ₆ bmt	1	100	100
LaCl ₃ ·7H ₂ O	4/24	27/71	93/93
1	4/24	10/80	100

^a Reaction conditions: PhEtO (0.41 mmol), catalyst (20 mg), alcohol (1 mL). ^b Conversion of PhEtO. ^c Selectivity to MeOPhEtOH.

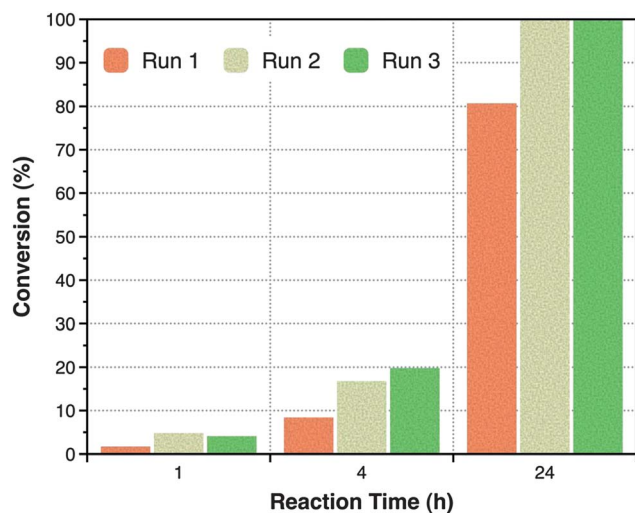


Fig. 9 Catalytic performance of compound $[\text{La}_2(\text{H}_3\text{bmt})_2(\text{H}_2\text{O})_2] \cdot \text{H}_2\text{O}$ (**1**) in three consecutive batch runs of the reaction of styrene oxide using methanol at 55 °C.

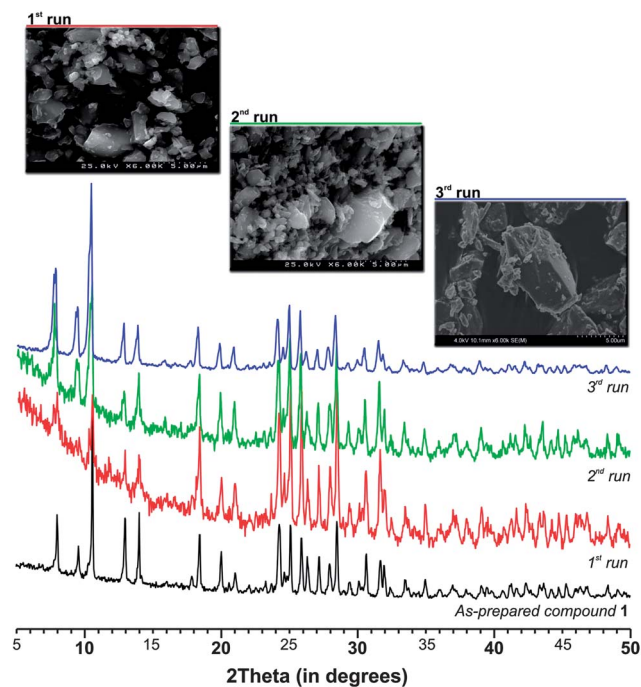


Fig. 10 Characterization (SEM imaging and powder X-ray diffraction) of the recovered $[\text{La}_2(\text{H}_3\text{bmt})_2(\text{H}_2\text{O})_2] \cdot \text{H}_2\text{O}$ (**1**) catalyst after each batch run. Results clearly indicate that the crystal structure of the material remains unaltered throughout the performed catalytic tests. For comparative purposes the PXRD pattern of the bulk material **1** is also depicted. *Please note:* the distinct signal-to-noise ratios of the PXRD patterns are a consequence of distinct acquisition periods.

seem to also lead to these compounds (tested for 1 day for the La^{3+} -based material). Remarkably, under microwave irradiation, temperature appeared to be a crucial element in the self-assembly process: for 5 minutes of reaction time, phase-pure materials can only be isolated for temperatures greater than 150 °C. These results clearly indicate that by systematically investigating the synthesis of this isotypical system of LnOFs it might be possible to derive optimal conditions to isolate them in the shortest possible period of time. Moreover, and based on our investigations on the use of microwave irradiation,³⁷ it might even be possible to control either crystal morphology or size, or even both, or even find new materials. These investigations are currently underway in our laboratories.

$[\text{Ln}_2(\text{H}_3\text{bmt})_2(\text{H}_2\text{O})_2] \cdot \text{H}_2\text{O}$ materials were found to be three-dimensional LnOFs, built up on a single crystallographically independent lanthanide center, trapping solvent water molecules (both of crystallization and coordinated to the lanthanide center). As expected, the anionic $\text{H}_3\text{bmt}^{3-}$ linker was found to be a rather robust organic PBU, leading to materials which exhibit a typical zeolitic behaviour: by heating or applying a high vacuum, all water molecules could be reversibly removed from the structures; this process was shown to occur without loss of crystallinity or modification of the overall topological features (both the as-prepared and dehydrated materials are novel binodal 6,6-connected architectures).

This typical zeolitic behaviour was found to have important consequences in the observed photoluminescent properties. Firstly, the removal of the water molecules from the Eu^{3+} -based

material leads to a concomitant increase of the quantum efficiency from *ca.* 15% (for the as-prepared compound) to *ca.* 54%. Secondly, the Tb³⁺ compound shows the remarkable absolute emission quantum yield of *ca.* 46% (at 280 nm excitation) reflecting a good balance between absorption, energy transfer and emission rates. The catalytic activity of the La³⁺-based material **1** was tested in the ring-opening reaction of styrene oxide with methanol, and it was found that: (i) the material acts as a truly heterogeneous catalyst; (ii) it exhibits an excellent regioselectivity towards 2-methoxy-2-phenylethanol, which is always the sole reaction product; (iii) it can be recycled by simple and efficient regeneration processes; and (iv) activity increases with the catalytic runs without a significant loss of crystallinity or modification of the crystal structure.

Future research in our laboratories, in particular that based on the use of H₆bmt as an organic linker precursor, will be as mentioned above focused at the optimization of the hydrothermal synthesis to reduce synthesis times and also reduce crystallite size. We note that these are two important requirements for the eventual use of these [Ln₂(H₃bmt)₂(H₂O)₂] \cdot H₂O materials in possible industrial applications and devices. Because H_{6-x}bmt^{x-} residues seem to be much better sensitizers than our previously employed organic tripodal linkers, future work will also be greatly devoted to the design of novel molecules so as to: (i) retain the observed energy-transfer efficiency for Tb³⁺; (ii) improve the photoluminescence properties of Eu³⁺, mainly by promoting a red-shift of the absorption band of the ligand so that the triplet states can also efficiently sensitize this optically active lanthanide; and (iii) build up on the increased structural robustness observed for the [Ln₂(H₃bmt)₂(H₂O)₂] \cdot H₂O materials and design ligands that can promote the existence of larger channels which may, for example, boost the catalytic activity or allow the selective adsorption of gases.

4. Materials and methods

4.1. General instrumentation

SEM (Scanning Electron Microscopy) images and EDS data were collected using either a Hitachi S-4100 field emission gun tungsten filament instrument working at 25 kV or a scanning electron microscope SU-70 working at 4 kV. Samples were prepared by deposition on aluminium sample holders followed by carbon coating. SEM mapping images were recorded using the microscope SU-70 working at 15 kV.

Thermogravimetric analyses (TGA) were carried out using a Shimadzu TGA 50, from room temperature to *ca.* 800 °C, at a heating rate of 5 °C min⁻¹, under a continuous stream of air at a flow rate of 20 mL min⁻¹.

Fourier Transform Infrared (FT-IR) spectra (in the range 3750–350 cm⁻¹) were recorded with KBr pellets (2 mg of the sample were mixed in a mortar with 200 mg of KBr) using a Bruker Tensor 27 spectrometer by averaging 200 scans at a maximum resolution of 2 cm⁻¹.

Elemental analyses for C, N and H were performed with a Truspec 630-200-200 elemental analyzer at the Department of Chemistry, University of Aveiro. Typical samples (between 1 and 2 mg) were combusted at 850 °C for 4 minutes under an oxygen atmosphere. Helium was used as the carrier gas.

Routine powder X-ray diffraction (PXRD) data for all synthesized materials were collected at ambient temperature on an X'Pert MPD Philips diffractometer, equipped with an X'Celerator detector and a flat-plate sample holder in a Bragg-Brentano para-focusing optics configuration (40 kV, 50 mA). Intensity data were collected by the step-counting method (step 0.04°), in continuous mode, in the *ca.* 5 ≤ 2θ ≤ 50° range.

¹³C CP MAS and ³¹P MAS spectra were recorded at 9.4 T on a Bruker Avance 400 wide-bore spectrometer (DSX model) on a 4 mm BL cross-polarization magic-angle spinning (CPMAS) VTN probe at 100.6 and 161.9 MHz, respectively. For the ¹³C {¹H} CP MAS spectra the Hartmann–Hahn (HH) “sideband” matching condition $\nu_1^{13\text{C}} = \nu_1^{1\text{H}} + n\nu_{\text{R}}$ ($n = \pm 1$) was carefully matched by calibrating the ¹H and the ¹³C *rf* field strengths; recycle delay: 5 s; contact time: 2 ms; $\nu_{\text{R}} = 12$ kHz. For the ³¹P HPDEC spectra a 90° single pulse excitation of 2.5 μs was employed; recycle delay: 60s; $\nu_{\text{R}} = 8$ kHz. Chemical shifts are quoted in parts per million with respect to TMS for the ¹³C nuclei, and to an 85% H₃PO₄ solution for the ³¹P nucleus.

¹H, ¹³C and ³¹P Nuclear Magnetic Resonance (NMR) spectra were recorded with a Bruker AVANCE 300 spectrometer at 300.13, 75.47 and 121.49 MHz, respectively. Deuterated chloroform (CDCl₃) and dimethylsulfoxide-d₆ (DMSO-d₆) were used as solvents, and tetramethylsilane or H₃PO₄ (85%) was used as the internal reference. Chemical shifts (δ) are quoted in ppm and the coupling constants (*J*) in Hz.

Mass spectra were collected using a Micromass Q-TOF2 equipment. Dichloromethane was used as the solvent for hexaethyl(benzene-1,3,5-triyltris(methylene))tris(phosphonate) (**L'**) and water for (benzene-1,3,5-triyltris(methylene))triphosphonic acid (**H₆bmt**). The employed concentration was 1 mg mL⁻¹. Samples were diluted in methanol to a concentration of 2 μL (sample)/200 μL (methanol).

4.2. Reagents

Chemicals were readily available from commercial sources and were used as received without further purification: lanthanide(III) chloride hydrates (LnCl₃ \cdot *x*H₂O, Ln³⁺ = La³⁺, Ce³⁺, Pr³⁺, Nd³⁺, Eu³⁺ and Tb³⁺; 99.9%, Sigma-Aldrich); 1,3,5-tris(bromomethyl)benzene (C₉H₉Br₃, 97%, Sigma-Aldrich); triethyl phosphite ((C₂H₅O)₃P, 98%, Sigma-Aldrich); styrene oxide (C₈H₈O, ≥97%, Fluka); hydrochloric acid (HCl, 37%, Panreac); dichloromethane (CH₂Cl₂, pure, Sigma-Aldrich); methanol (CH₃OH, >99.8% from Fluka, or 99% from Sigma-Aldrich); *n*-hexane (>99%, Sigma-Aldrich); dimethylsulfoxide-d₆ (DMSO-d₆, 99.99%, Euriso-top); and deuterated chloroform (CDCl₃, 99.99%, Euriso-top). All yields are cited based on mol%.

4.3. Synthesis of (benzene-1,3,5-triyltris(methylene))triphosphonic acid

A mixture of 1,3,5-tris(bromomethyl)benzene (0.3 g, 0.84 mmol) and triethyl phosphite (5 mL) was allowed to react under nitrogen atmosphere and at 120 °C for approximately 12 h. After cooling to ambient temperature the excess of triethyl phosphite was removed by distillation under reduced pressure. The resulting orange oil residue was dissolved in dichloromethane and the intermediate **L'** was purified by flash column chromatography

using a mixture of dichloromethane and methanol (95 : 5) as eluent. **L'** was isolated as a colorless oil in 88% yield.

Intermediate **L'** (0.47 g, 0.89 mmol) was transferred into an aqueous solution of HCl (30 mL, 6 M) and the reaction mixture was then refluxed for approximately 20 h under continuous magnetic stirring. The reaction product was washed with dichloromethane and the aqueous phase was distilled under reduced pressure. The resulting compound, (benzene-1,3,5-triyltris(methylene))triphosphonic acid (**H₆bmt**), was recovered as a white solid by vacuum filtration and was washed with copious amounts of acetone. Yield: 92%.

L': ¹H NMR (300.13 MHz, CDCl₃) δ: 1.22 (t, 18H, *J*(¹H–¹H) = 7.1 Hz, CH₃), 3.08 (d, 6H, *J*(¹H–³¹P) = 22.1 Hz, CH₂PO₃Et₂), 4.00 (dq, 12H, *J*(¹H–¹H) = 7.2 Hz and *J*(¹H–³¹P) = 7.9 Hz, CH₂CH₃) and 7.10 (dt, 3H, *J*(¹H–¹H) = *J*(¹H–³¹P) = 2.4 Hz, Ar–H). ¹³C NMR (75.47 MHz, CDCl₃) δ: 16.2–16.3 (CH₃), 33.3 (d, *J*(¹³C–³¹P) = 138.0 Hz, CH₂PO₃Et₂), 62.0–62.1 (CH₂CH₃), 129.7 (dt, *J*(¹³C–³¹P) = 5.8 Hz and *J*(¹³C–³¹P) = 5.2 Hz, Ar–CH) and 131.9–132.1 (Ar–C). MS (TOF MS ES⁺) *m/z*: 529.2 (M + H)⁺ and 551.1 (M + Na)⁺.

H₆bmt: ¹H NMR (300.13 MHz, DMSO-*d*₆) δ: 2.87 (d, 6H, *J*(¹H–³¹P) = 21.8 Hz, CH₂) and 7.01 (d, 3H, *J*(¹H–¹H) = 1.95 Hz, Ar–H). ¹³C NMR (75.47 MHz, DMSO-*d*₆) δ: 35.2 (*J*(¹³C–³¹P) = 132.6 Hz, CH₂), 129.0 (Ar–CH) and 133.5 (Ar–C). ³¹P NMR (121.49 MHz, DMSO-*d*₆) δ: 22.5 (t, *J*(³¹P–¹H) = 21.2 Hz, PO₃H₂). MS (TOF MS ES⁻) *m/z*: 359.0 (M – H)⁻.

4.4. Hydrothermal synthesis of [Ln₂(H₃bmt)₂(H₂O)₂]·H₂O

Mixtures of the respective lanthanide(III) chloride hydrates [LnCl₃·*n*H₂O, where Ln³⁺ = La³⁺ (**1**), Ce³⁺ (**2**), Pr³⁺ (**3**), and Nd³⁺ (**4**)] and (benzene-1,3,5-triyltris(methylene))triphosphonic acid (**H₆bmt**) were prepared in distilled water (*ca.* 6 mL) with a molar ratio of approximately 1 : 2 : 1800 (**H₆bmt** : Ln³⁺ : H₂O), respectively (for **1**, 0.0666 g of **H₆bmt** was reacted with 0.1374 g of LaCl₃·7H₂O). The mixtures were kept under constant magnetic stirring and atmospheric conditions for approximately 30 min. The resulting suspensions were transferred to Teflon-lined Parr Instrument autoclaves and placed inside a pre-heated MMM Venticell oven where they remained at 180 °C for a period of 72 h. After the reaction, the vessels were allowed to cool slowly to ambient temperature and the resulting materials (typically white microcrystalline powders) were recovered by vacuum filtration, washed with abundant amounts of distilled water and air-dried at ambient temperature.

The mixed-lanthanide materials with 5% of Eu³⁺ (**5**) or 5% of Tb³⁺ (**6**) dispersed in a La³⁺ matrix were prepared following the aforementioned procedure while adjusting the amounts of the lanthanide chloride salts to the desired amounts.

Elemental CH composition (%). Calcd for **1**: C 20.70; H 2.89. Found: C 20.50; H 2.84. Calcd for **2**: C 20.60; H 2.88. Found: C 20.90; H 2.80. Calcd for **3**: C 20.60; H 2.88. Found: C 21.10; H 2.82. Calcd for **4**: C 20.50; H 2.86. Found: C 20.80; H 2.79. Calcd for **5**: C 20.60; H 2.89. Found: C 20.60; H 2.78. Calcd for **6**: C 20.60; H 2.89. Found: C 20.50; H 2.85.

Thermogravimetric analysis (TGA) data (weight losses in %) and derivative thermogravimetric peaks (DTG; in italics inside the parentheses). **1**: 38–130 °C – 1.4% (69 °C); 130–265 °C – 3.5% (162 °C); 350–565 °C – 4.7% (458 °C). **2**: 31–106 °C – 1.4%

(50 °C); 106–270 °C – 3.0% (159 °C); 366–521 °C – 4.2% (472 °C). **3**: 35–107 °C – 1.2% (51 °C); 107–280 °C – 2.7% (154 °C); 417–560 °C – 3.9% (477 °C). **4**: 32–99 °C – 1.5% (54 °C); 99–270 °C – 3.1% (148 °C); 360–578 °C – 4.7% (486 °C). **5**: 44–121 °C – 1.2% (53 °C); 121–263 °C – 3.2% (162 °C); 373–555 °C – 4.4% (465 °C). **6**: 50–142 °C – 0.8% (63 °C); 142–267 °C – 2.2% (157 °C); 441–506 °C – 3.2% (471 °C).

Selected FT-IR data (in cm⁻¹; from KBr pellets). **1**: $\nu(\text{H}_2\text{O})_{\text{coord}} = 3588\text{m}$; $\nu(\text{POH}) = 3420\text{m}$; $\nu(\text{H}_2\text{O})_{\text{cryst}}$ and $\nu(-\text{CH}_2-)$ = 3180–2820w; $\delta(\text{H}_2\text{O}) = 1605\text{m}$; $\delta(\text{POH}) = 1122\text{vs}$ and 1069vs. **2**: $\nu(\text{H}_2\text{O})_{\text{coord}} = 3588\text{m}$; $\nu(\text{POH}) = 3413\text{m}$; $\nu(\text{H}_2\text{O})_{\text{cryst}}$ and $\nu(-\text{CH}_2-)$ = 3190–2750w; $\delta(\text{H}_2\text{O}) = 1605\text{m}$; $\delta(\text{POH}) = 1119\text{vs}$ and 1069vs. **3**: $\nu(\text{H}_2\text{O})_{\text{coord}} = 3589\text{m}$; $\nu(\text{POH}) = 3412\text{m}$; $\nu(\text{H}_2\text{O})_{\text{cryst}}$ and $\nu(-\text{CH}_2-)$ = 3190–2750w; $\delta(\text{H}_2\text{O}) = 1605\text{m}$; $\delta(\text{POH}) = 1120\text{vs}$ and 1067vs. **4**: $\nu(\text{H}_2\text{O})_{\text{coord}} = 3589\text{m}$; $\nu(\text{POH}) = 3410\text{m}$; $\nu(\text{H}_2\text{O})_{\text{cryst}}$ and $\nu(-\text{CH}_2-)$ = 3190–2750w; $\delta(\text{H}_2\text{O}) = 1605\text{m}$; $\delta(\text{POH}) = 1122\text{vs}$ and 1067vs. **5**: $\nu(\text{H}_2\text{O})_{\text{coord}} = 3588\text{m}$; $\nu(\text{POH}) = 3414\text{m}$; $\nu(\text{H}_2\text{O})_{\text{cryst}}$ and $\nu(-\text{CH}_2-)$ = 3190–2750w; $\delta(\text{H}_2\text{O}) = 1605\text{m}$; $\delta(\text{POH}) = 1120\text{vs}$ and 1069vs. **6**: $\nu(\text{H}_2\text{O})_{\text{coord}} = 3589\text{m}$; $\nu(\text{POH}) = 3415\text{m}$; $\nu(\text{H}_2\text{O})_{\text{cryst}}$ and $\nu(-\text{CH}_2-)$ = 3190–2750w; $\delta(\text{H}_2\text{O}) = 1605\text{m}$; $\delta(\text{POH}) = 1119\text{vs}$ and 1069vs.

4.5. Microwave-assisted synthesis of [La₂(H₃bmt)₂(H₂O)₂]·H₂O

A mixture containing 0.1374 g of LaCl₃·7H₂O and 0.0666 g of **H₆bmt** was prepared at ambient temperature in *ca.* 6 mL of distilled water, with an overall molar ratio of *ca.* 2 : 1 : 1800 (La³⁺ : **H₆bmt** : H₂O), directly inside a 10 mL IntelliVent microwave reactor. Reaction occurred inside a CEM Focused Microwave Synthesis System Discover S-Class equipment, using an irradiation power of 50 W and a reaction time of 5 min. The maximum temperature reached was varied between 120 and 150 °C. The reaction mixture was kept under constant magnetic stirring throughout the synthesis and a constant flow of air (*ca.* 20–30 psi of pressure) ensured a close control of the temperature inside the reactor. The final product was recovered by vacuum filtration, washed with abundant amounts of distilled water and then air-dried at ambient temperature. Phase identification was performed using powder X-ray diffraction.

4.6. Single-crystal X-ray diffraction studies

Suitable single-crystals of [Ln₂(H₃bmt)₂(H₂O)₂]·H₂O materials [where Ln³⁺ = La³⁺ (**1**), Ce³⁺ (**2**), Pr³⁺ (**3**), and Nd³⁺ (**4**)] were manually selected from the crystallization vials and were mounted on a Hampton Research CryoLoops³⁸ with the help of a highly viscous FOMBLIN Y perfluoropolyether vacuum oil (LVAC 140/13; purchased from Sigma-Aldrich) and a Stemi 2000 stereomicroscope equipped with Carl Zeiss lenses. The dehydrated [La(H₃bmt)] (**1-dehyd**) material was isolated from the as-prepared compound **1** by placing it inside an oven at 230 °C over a period of 12 hours. To avoid rehydration, crystals at this temperature were immediately immersed in the aforementioned FOMBLIN oil, selected and mounted into the single-crystal X-ray diffractometer. Data were collected at low temperature on a Bruker X8 Kappa APEX II charge-coupled device (CCD) area-detector diffractometer (Mo K_α graphite-monochromated

radiation, $\lambda = 0.71073 \text{ \AA}$) controlled by the APEX2 software package,³⁹ and equipped with an Oxford Cryosystems Series 700 cryostream monitored remotely using the software interface Cryopad.⁴⁰ Images were processed using the software package SAINT+,⁴¹ and data were corrected for absorption by the multi-scan semi-empirical method implemented in SADABS.⁴² Structures were solved using the direct methods algorithm implemented in SHELXS-97,⁴³ which allowed the immediate location of the majority of the atoms, in particular the central metallic nodes and the phosphorous atoms. All remaining non-hydrogen atoms were located from difference Fourier maps calculated from successive full-matrix least squares refinement cycles on F^2 using SHELXL-97.^{43b,44}

In compounds **1** to **4** the coordination sphere of the Ln^{3+} centre contains a water molecule. In **1**, **2**, and **4** this water molecule is affected by positional disorder and it was modelled over two distinct crystallographic positions with a fixed rate of occupancy of 50% for each. The hydrogen atoms associated with these water molecules were markedly visible in difference Fourier maps and were included in the final structural model as occupying the same location for the two positions of the coordinated oxygen atoms. In order to ensure a chemically reasonable geometry for these coordinated moieties the O–H and H...H distances were restrained to 0.95(1) and 1.55(1) \AA , respectively. The isotropic thermal displacement parameters (U_{iso}) of these oxygen atoms were fixed at 1.5 times U_{eq} of the oxygen atom to which they are attached. In compound **3** (with Pr^{3+}) this disorder was not visible and the coordination sphere of Pr^{3+} only has a single location for the coordinated water molecule.

In all structures a single crystallographically independent oxygen atom associated with a water molecule of crystallization was found in the small cavities present in the crystal structure. This molecule was ultimately included in the final structural models with a fixed occupancy of 50%. Even though this molecule could be refined by assuming an anisotropic displacement behaviour, the hydrogen atoms associated with this moiety could not be located either from difference Fourier maps or in calculated positions. Nevertheless these hydrogen atoms have been included in the empirical formulae of the materials (see Table 1).

Hydrogen atoms bound to carbon and the PO–H phosphonate groups were placed in idealized positions using appropriate *HFIX* instructions in SHELXL (43 for the aromatic atoms, 23 for the $-\text{CH}_2-$ moieties and 147 for the PO–H groups) and included in subsequent refinement cycles in riding-motion approximation with isotropic thermal displacement parameters (U_{iso}) fixed at 1.2 or 1.5 (only for the latter moieties) times U_{eq} of the carbon atom to which they are attached.

The last difference Fourier map synthesis showed: for **1**, the highest peak (0.690 e\AA^{-3}) and deepest hole (-0.722 e\AA^{-3}) located at 0.83 \AA and 0.51 \AA from O5 and P3, respectively; for **1-dehyd**, the highest peak (2.426 e\AA^{-3}) and deepest hole (-0.887 e\AA^{-3}) located at 0.66 \AA and 0.53 \AA from La1, respectively; for **2**, the highest peak (0.486 e\AA^{-3}) and deepest hole (-0.612 e\AA^{-3}) located at 0.98 \AA and 0.23 \AA from Ce1 and H2, respectively; for **3**, the highest peak (1.537 e\AA^{-3}) and deepest hole (-1.756 e\AA^{-3}) located at 1.10 \AA and 0.85 \AA from Pr1, respectively; for **4**, the highest peak (1.036 e\AA^{-3}) and deepest hole (-1.188 e\AA^{-3}) located at 1.92 \AA and 0.98 \AA from O7 and Nd1, respectively. Information concerning crystallographic data

collection and structure refinement details is summarized in Table 1. Selected bond lengths and angles for the La^{3+} coordination environments in **1** and **1-dehyd** are displayed in Tables 2 and 3, respectively. Structural drawings have been created using the software package Crystal Diamond.⁴⁵

4.7. Variable temperature powder X-ray diffraction

Variable-temperature powder X-ray diffraction data for $[\text{La}_2(\text{H}_3\text{bmt})_2(\text{H}_2\text{O})_2] \cdot \text{H}_2\text{O}$ (**1**) were collected on an X'Pert MPD Philips diffractometer (Cu K_{α} X-radiation, $\lambda = 1.54060 \text{ \AA}$) under air atmosphere, equipped with an X'Celerator detector, a curved graphite-monochromated radiation, a flat-plate sample holder in a Bragg–Brentano para-focusing optics configuration (40 kV, 50 mA), and a high-temperature Antoon Parr HKL 16 chamber controlled by an Antoon Parr 100 TCU unit. Intensity data were collected in the step mode (0.03° , 2 seconds per step) in the range of $ca. 5 \leq 2\theta \leq 35^\circ$. Data were collected between 30°C and 700°C .

4.8. Photoluminescence

Emission and excitation spectra were recorded on a Fluorolog-2® Horiba Scientific (Model FL3-2T) spectroscopy, with a modular double grating excitation spectrometer (fitted with a 1200 grooves per mm grating blazed at 330 nm) and a TRIAX 320 single emission monochromator (fitted with a 1200 grooves per mm grating blazed at 500 nm; reciprocal linear density of 2.6 nm mm^{-1}), coupled to a R928 Hamamatsu photomultiplier, using the front face acquisition mode. The excitation source was a 450 W Xe arc lamp. Emission spectra were corrected for detection and optical spectral response of the spectrofluorimeter and the excitation spectra were corrected for the spectral distribution of the lamp intensity using a photodiode reference detector. Time-resolved measurements have been carried out using a 1934D3 phosphorimeter coupled with the Fluorolog®-3, and a Xe–Hg flash lamp (6 μs per pulse half width and 20–30 μs tail) was used as the excitation source. The variable temperature measurements were performed using a helium-closed cycle cryostat with a vacuum system measuring $\sim 5 \times 10^{-6}$ mbar and a Lakeshore 330 auto-tuning temperature controller with a resistance heater. The temperature can be adjusted from 11 to 450 K.

The absolute emission quantum yields were measured at ambient temperature using a quantum yield measurement system C9920-02 from Hamamatsu with a 150 W xenon lamp coupled to a monochromator for wavelength discrimination, an integrating sphere as sample chamber and a multi-channel analyzer for signal detection. Three measurements were made for each sample so that the average value is reported. The method is accurate to within 10%.

4.9. Heterogeneous catalysis

A 5 mL borosilicate batch reactor equipped with a magnetic stirrer and a valve for sampling was charged with 20 mg of catalyst $[\text{La}_2(\text{H}_3\text{bmt})_2(\text{H}_2\text{O})_2] \cdot \text{H}_2\text{O}$ (**1**), 1 mL of methanol and 0.41 mmol (0.048 mL) of styrene oxide. The reaction was carried out under atmospheric air, with the batch reactor immersed in an external thermostated oil bath. Replicas of the catalytic experiments were performed so as to ensure reproducibility of the

reported results. The progress of the heterogeneous catalytic reactions was monitored using a Varian 3900 GC equipped with a capillary column (SPB-5, 20 m × 0.25 mm) and a flame ionization detector (using mesitylene as an internal standard). Reaction products were identified by GC-MS (Trace GC 2000 Series (Thermo Quest CE Instruments) – DSQ II (Thermo Scientific)), using He as the carrier gas.

Acknowledgements

We would like to thank *Fundação para a Ciência e a Tecnologia* (FCT, Portugal), the European Union, QREN, FEDER, COMPETE and *Laboratório Associado Centro de Investigação em Materiais Cerâmicos e Compósitos*, CICECO (PEst-C/CTM/LA0011/2011), for their general funding scheme. We further wish to thank FCT for funding the R&D project PTDC/QUI-QUI/098098/2008 (FCOMP-01-0124-FEDER-010785), for specific funding towards the purchase of the single-crystal diffractometer, and for the doctoral research grant no. SFRH/BD/66371/2009 (to SMFV).

References

- (a) M. Eddaoudi, D. B. Moler, H. L. Li, B. L. Chen, T. M. Reineke, M. O'Keeffe and O. M. Yaghi, *Acc. Chem. Res.*, 2001, **34**, 319–330; (b) S. R. Batten and R. Robson, *Angew. Chem., Int. Ed.*, 1998, **37**, 1460–1494; (c) S. Kitagawa, R. Kitaura and S. Noro, *Angew. Chem., Int. Ed.*, 2004, **43**, 2334–2375; (d) C. Janiak, *Dalton Trans.*, 2003, 2781–2804; (e) H. Li, M. Eddaoudi, M. O'Keeffe and O. M. Yaghi, *Nature*, 1999, **402**, 276–279; (f) O. M. Yaghi, M. O'Keeffe, N. W. Ockwig, H. K. Chae, M. Eddaoudi and J. Kim, *Nature*, 2003, **423**, 705–714; (g) M. Eddaoudi, J. Kim, N. Rosi, D. Vodak, J. Wachter, M. O'Keeffe and O. M. Yaghi, *Science*, 2002, **295**, 469–472.
- (a) M. O'Keeffe and O. M. Yaghi, *Chem. Rev.*, 2012, **112**, 675–702; (b) E. V. Alexandrov, V. A. Blatov, A. V. Kochetkov and D. M. Proserpio, *CrystEngComm*, 2011, **13**, 3947–3958.
- A. U. Czaja, N. Trukhan and U. Muller, *Chem. Soc. Rev.*, 2009, **38**, 1284–1293.
- (a) S. C. Xiang, Z. J. Zhang, C. G. Zhao, K. L. Hong, X. B. Zhao, D. R. Ding, M. H. Xie, C. D. Wu, M. C. Das, R. Gill, K. M. Thomas and B. L. Chen, *Nat. Commun.*, 2011, **2**, 204; (b) Y. S. Bae, C. Y. Lee, K. C. Kim, O. K. Farha, P. Nickias, J. T. Hupp, S. T. Nguyen and R. Q. Snurr, *Angew. Chem., Int. Ed.*, 2012, **51**, 1857–1860; (c) S. A. FitzGerald, B. Burkholder, M. Friedman, J. B. Hopkins, C. J. Pierce, J. M. Schloss, B. Thompson and J. L. C. Rowsell, *J. Am. Chem. Soc.*, 2011, **133**, 20310–20318; (d) J. Yang, A. Grzech, F. M. Mulder and T. J. Dingemans, *Chem. Commun.*, 2011, **47**, 5244–5246; (e) K. Suh, M. P. Yutkin, D. N. Dybtsev, V. P. Fedin and K. Kim, *Chem. Commun.*, 2012, **48**, 513–515; (f) B. Z. Yuan, D. Y. Ma, X. Wang, Z. Li, Y. W. Li, H. M. Liu and D. H. He, *Chem. Commun.*, 2012, **48**, 1135–1137; (g) N. L. Rosi, J. Eckert, M. Eddaoudi, D. T. Vodak, J. Kim, M. O'Keeffe and O. M. Yaghi, *Science*, 2003, **300**, 1127–1129.
- (a) A. Bétard and R. A. Fischer, *Chem. Rev.*, 2012, **112**, 1055–1083; (b) B. Liu, O. Shekhan, H. K. Arslan, J. X. Liu, C. Woll and R. A. Fischer, *Angew. Chem., Int. Ed.*, 2012, **51**, 807–810; (c) C. Pan, J. P. Nan, X. L. Dong, X. M. Ren and W. Q. Jin, *J. Am. Chem. Soc.*, 2011, **133**, 12330–12333; (d) X. L. Liu, Y. S. Li, G. Q. Zhu, Y. J. Ban, L. Y. Xu and W. S. Yang, *Angew. Chem., Int. Ed.*, 2011, **50**, 10636–10639.
- (a) F. Ke, Y. P. Yuan, L. G. Qiu, Y. H. Shen, A. J. Xie, J. F. Zhu, X. Y. Tian and L. D. Zhang, *J. Mater. Chem.*, 2011, **21**, 3843–3848; (b) P. Horcajada, R. Gref, T. Baati, P. K. Allan, G. Maurin, P. Couvreur, G. Férey, R. E. Morris and C. Serre, *Chem. Rev.*, 2012, **112**, 1232–1268; (c) D. M. Liu, S. A. Kramer, R. C. Huxford-Phillips, S. Z. Wang, J. Della Rocca and W. B. Lin, *Chem. Commun.*, 2012, **48**, 2668–2670; (d) D. M. Liu, R. C. Huxford and W. B. Lin, *Angew. Chem., Int. Ed.*, 2011, **50**, 3696–3700.
- (a) J. Rocha, L. D. Carlos, F. A. A. Paz and D. Ananias, *Chem. Soc. Rev.*, 2011, **40**, 926–940; (b) D. Maspocho, N. Domingo, D. R. Molina, K. Wurst, J. M. Hernandez, G. Vaughan, C. Rovira, F. Lloret, J. Tejada and J. Veciana, *Chem. Commun.*, 2005, 5035–5037; (c) D. Maspocho, D. Ruiz-Molina and J. Veciana, *J. Mater. Chem.*, 2004, **14**, 2713–2723; (d) D. Maspocho, D. Ruiz-Molina and J. Veciana, *Chem. Soc. Rev.*, 2007, **36**, 770–818; (e) D. W. Ryu, W. R. Lee, J. W. Lee, J. H. Yoon, H. C. Kim, E. K. Koh and C. S. Hong, *Chem. Commun.*, 2010, **46**, 8779–8781; (f) H. Tian, Q. X. Jia, E. Q. Gao and Q. L. Wang, *Chem. Commun.*, 2010, **46**, 5349–5351; (g) X. L. Tong, T. L. Hu, J. P. Zhao, Y. K. Wang, H. Zhang and X. H. Bu, *Chem. Commun.*, 2010, **46**, 8543–8545; (h) E. Pardo, C. Train, G. Gontard, K. Boubekeur, O. Fabelo, H. B. Liu, B. Dkhil, F. Lloret, K. Nakagawa, H. Tokoro, S. Ohkoshi and M. Verdaguer, *J. Am. Chem. Soc.*, 2011, **133**, 15328–15331; (i) J. He, M. Zeller, A. D. Hunter and Z. T. Xu, *J. Am. Chem. Soc.*, 2012, **134**, 1553–1559.
- (a) A. Dhakshinamoorthy, M. Alvaro and H. Garcia, *Chem.–Eur. J.*, 2010, **16**, 8530–8536; (b) F. J. Song, C. Wang and W. B. Lin, *Chem. Commun.*, 2011, **47**, 8256–8258; (c) J. M. Falkowski, C. Wang, S. Liu and W. B. Lin, *Angew. Chem., Int. Ed.*, 2011, **50**, 8674–8678; (d) C. Chizallet, S. Lazare, D. Bazer-Bachi, F. Bonnier, V. Lecocq, E. Soyer, A. A. Quoineaud and N. Bats, *J. Am. Chem. Soc.*, 2010, **132**, 12365–12377; (e) A. Corma, H. Garcia and F. X. L. Xamena, *Chem. Rev.*, 2010, **110**, 4606–4655; (f) D. B. Dang, P. Y. Wu, C. He, Z. Xie and C. Y. Duan, *J. Am. Chem. Soc.*, 2010, **132**, 14321–14323; (g) H. H. Fei, D. L. Rogow and S. R. J. Oliver, *J. Am. Chem. Soc.*, 2010, **132**, 7202–7209; (h) J. Lee, O. K. Farha, J. Roberts, K. A. Scheidt, S. T. Nguyen and J. T. Hupp, *Chem. Soc. Rev.*, 2009, **38**, 1450–1459; (i) L. Q. Ma, C. Abney and W. B. Lin, *Chem. Soc. Rev.*, 2009, **38**, 1248–1256; (j) P. K. Thallapally, C. A. Fernandez, R. K. Motkuri, S. K. Nune, J. Liu and C. H. F. Peden, *Dalton Trans.*, 2010, **39**, 1692–1694; (k) J. S. Seo, D. Whang, H. Lee, S. I. Jun, J. Oh, Y. J. Jeon and K. Kim, *Nature*, 2000, **404**, 982–986.
- N. C. Jeong, B. Samanta, C. Y. Lee, O. K. Farha and J. T. Hupp, *J. Am. Chem. Soc.*, 2012, **134**, 51–54.
- B. H. Ye, M. L. Tong and X. M. Chen, *Coord. Chem. Rev.*, 2005, **249**, 545–565.
- O. Guillou and C. Daiguebonne, *Lanthanide-Containing Coordination Polymers in Handbook on the Physics and Chemistry of Rare Earths*, ed. K. A. Gschneidner, J.-C. G. Bunzli and V. K. Pecharsky, Elsevier B. V., 2005, pp. 359–404.
- G. K. H. Shimizu, R. Vaidhyanathan and J. M. Taylor, *Chem. Soc. Rev.*, 2009, **38**, 1430–1449.
- (a) P. Silva, F. Vieira, A. C. Gomes, D. Ananias, J. Fernandes, S. M. Bruno, R. Soares, A. A. Valente, J. Rocha and F. A. A. Paz, *J. Am. Chem. Soc.*, 2011, **133**, 15120–15138; (b) J. Rocha, F. A. A. Paz, F. N. Shi, D. Ananias, N. J. O. Silva, L. D. Carlos and T. Trindade, *Eur. J. Inorg. Chem.*, 2011, 2035–2044; (c) P. Silva, A. A. Valente, J. Rocha and F. A. A. Paz, *Cryst. Growth Des.*, 2010, **10**, 2025–2028; (d) J. Rocha, F. A. A. Paz, F. N. Shi, R. A. S. Ferreira, T. Trindade and L. D. Carlos, *Eur. J. Inorg. Chem.*, 2009, 4931–4945; (e) F. N. Shi, L. Cunha-Silva, T. Trindade, F. A. A. Paz and J. Rocha, *Cryst. Growth Des.*, 2009, **9**, 2098–2109; (f) F. N. Shi, L. Cunha-Silva, R. A. S. Ferreira, L. Mafrá, T. Trindade, L. D. Carlos, F. A. A. Paz and J. Rocha, *J. Am. Chem. Soc.*, 2008, **130**, 150–167; (g) F. N. Shi, T. Trindade, J. Rocha and F. A. A. Paz, *Cryst. Growth Des.*, 2008, **8**, 3917–3920.
- F. A. A. Paz, J. Klinowski, S. M. F. Vilela, J. P. C. Tome, J. A. S. Cavaleiro and J. Rocha, *Chem. Soc. Rev.*, 2012, **41**, 1088–1110.
- (a) P. A. Jaffrès, D. Villemin, V. Montouillout, C. Fernandez, J. Chardon and J. S. D. Santos, *Mol. Cryst. Liq. Cryst.*, 2002, **389**, 87–95; (b) J. Zon, D. Y. Kong, K. Gagnon, H. Perry, L. Holliness and A. Clearfield, *Dalton Trans.*, 2010, **39**, 11008–11018; (c) J. Fawcett, A. W. G. Platt and S. Vickers, *Polyhedron*, 2003, **22**, 1431–1435; (d) R. Murugavel and M. P. Singh, *New J. Chem.*, 2010, **34**, 1846–1854; (e) C. I. Yang, Y. T. Song, Y. J. Yeh, Y. H. Liu, T. W. Tseng and K. L. Lu, *CrystEngComm*, 2011, **13**, 2678–2686.
- F. A. A. Paz and J. Klinowski, *J. Phys. Org. Chem.*, 2003, **16**, 772–782.
- (a) F. N. Shi, F. A. A. Paz, P. Girginova, J. Rocha, V. S. Amaral, J. Klinowski and T. Trindade, *J. Mol. Struct.*, 2006, **789**, 200–208;

- (b) F. N. Shi, F. A. A. Paz, P. I. Girginova, L. Mafra, V. S. Amaral, J. Rocha, A. Makal, K. Wozniak, J. Klinowski and T. Trindade, *J. Mol. Struct.*, 2005, **754**, 51–60; (c) F. A. A. Paz, J. Rocha, J. Klinowski, T. Trindade, F. N. Shi and L. Mafra, *Prog. Solid State Chem.*, 2005, **33**, 113–125; (d) F. A. A. Paz, F. N. Shi, J. Klinowski, J. Rocha and T. Trindade, *Eur. J. Inorg. Chem.*, 2004, 2759–2768; (e) F. A. A. Paz and J. Rocha, *N-(Phosphonomethyl) iminodiacetic Acid in the Construction of Coordination Polymers in Metal Phosphonate Chemistry: From Synthesis to Applications*, ed. A. Clearfield and K. Demadis, Royal Society of Chemistry, Cambridge, 2012, pp. 551–585.
- 18 (a) L. Cunha-Silva, D. Ananias, L. D. Carlos, F. A. A. Paz and J. Rocha, *Z. Kristallogr.*, 2009, **224**, 261–272; (b) L. Cunha-Silva, S. Lima, D. Ananias, P. Silva, L. Mafra, L. D. Carlos, M. Pillinger, A. A. Valente, F. A. A. Paz and J. Rocha, *J. Mater. Chem.*, 2009, **19**, 2618–2632.
- 19 L. Cunha-Silva, L. Mafra, D. Ananias, L. D. Carlos, J. Rocha and F. A. A. Paz, *Chem. Mater.*, 2007, **19**, 3527–3538.
- 20 (a) A. Winter, C. Friebe, M. D. Hager and U. S. Schubert, *Eur. J. Org. Chem.*, 2009, 801–809; (b) J. S. D. Santos, V. Montouillout, F. Fayon, C. Fernandez, L. Delain-Bioton, D. Villemin and P. A. Jaffres, *New J. Chem.*, 2004, **28**, 1244–1249.
- 21 J. A. Fernandes, S. M. F. Vilela, P. J. A. Ribeiro-Claro and F. A. A. Paz, *Acta Crystallogr., Sect. C: Cryst. Struct. Commun.*, 2011, **67**, o198–o200.
- 22 E. Díez-Barra, J. C. García-Martínez, S. Merino, R. del Rey, J. Rodríguez-López, P. Sanchez-Verdú and J. Tejada, *J. Org. Chem.*, 2001, **66**, 5664–5670.
- 23 A. Ben Akacha, S. Barkallah and H. Zantour, *Magn. Reson. Chem.*, 1999, **37**, 916–920.
- 24 G. Socrates, *Infrared Characteristic Group Frequencies – Tables and Charts*, John Wiley & Sons Ltd, Baffins Lane, Chichester, 1994.
- 25 (a) L. Carlucci, G. Ciani and D. M. Proserpio, *CrystEngComm*, 2003, **5**, 269–279; (b) I. A. Baburin, V. A. Blatov, L. Carlucci, G. Ciani and D. M. Proserpio, *J. Solid State Chem.*, 2005, **178**, 2452–2474; (c) O. Delgado-Friedrichs, M. D. Foster, M. O’Keeffe, D. M. Proserpio, M. M. J. Treacy and O. M. Yaghi, *J. Solid State Chem.*, 2005, **178**, 2533–2554; (d) L. Carlucci, G. Ciani and D. M. Proserpio, *Coord. Chem. Rev.*, 2003, **246**, 247–289.
- 26 (a) V. A. Blatov and A. P. Shevchenko, *TOPOS – Version 4.0 Professional (Beta Evaluation)*, Samara State University, Samara, Russia, 2006; (b) V. A. Blatov, A. P. Shevchenko and V. N. Serezhkin, *J. Appl. Crystallogr.*, 2000, **33**, 1193.
- 27 RCSR (Reticular Chemistry Structure Resource), Website: <http://rcsr.anu.edu.au/>.
- 28 S. T. Hyde, O. Delgado-Friedrichs, S. J. Ramsden and V. Robins, *Solid State Sci.*, 2006, **8**, 740.
- 29 D. Ananias, M. Kostova, F. A. A. Paz, A. Ferreira, L. D. Carlos, J. Klinowski and J. Rocha, *J. Am. Chem. Soc.*, 2004, **126**, 10410–10417.
- 30 (a) M. H. V. Werts, R. T. F. Jukes and J. W. Verhoeven, *Phys. Chem. Chem. Phys.*, 2002, **4**, 1542–1548; (b) L. D. Carlos, Y. Messaddeq, H. F. Brito, R. A. S. Ferreira, V. D. Bermudez and S. J. L. Ribeiro, H. F. Brito, R. A. S. Ferreira, V. D. Bermudez and S. J. L. Ribeiro, M. A. C. Santos, L. C. Thompson and N. K. Ito, *J. Lumin.*, 1996, **69**, 77–84; (c) O. L. Malta, H. F. Brito, J. F. S. Menezes, F. Silva, S. Alves, F. S. Farias and A. V. M. Andrade, *J. Lumin.*, 1997, **75**, 255–268; (d) O. L. Malta, M. A. C. Santos, L. C. Thompson and N. K. Ito, *J. Lumin.*, 1996, **69**, 77–84; (e) M. F. Hazenkamp and G. Blasse, *Chem. Mater.*, 1990, **2**, 105–110; (f) L. D. Carlos, R. A. S. Ferreira, V. D. Bermudez and S. J. L. Ribeiro, *Adv. Mater.*, 2009, **21**, 509–534.
- 31 T. Kimura and Y. Kato, *J. Alloys Compd.*, 1995, **225**, 284–287.
- 32 F. A. Dias, L. D. Carlos, Y. Messaddeq and S. J. L. Ribeiro, *Langmuir*, 2005, **21**, 1776–1783.
- 33 D. Jiang, T. Mallat, F. Krumeich and A. Baiker, *J. Catal.*, 2008, **257**, 390–395.
- 34 T. Weil, M. Kotke, C. M. Kleiner and P. R. Schreiner, *Org. Lett.*, 2008, **10**, 1513–1516.
- 35 (a) V. Mirkhani, S. Tangestaninejad, B. Yadollahi and L. Alipanah, *Tetrahedron*, 2003, **59**, 8213–8218; (b) N. Iranpoor, M. Shekarriz and F. Shiriny, *Synth. Commun.*, 1998, **28**, 347–366.
- 36 G. Sabitha, R. S. Babu, M. Rajkumar, C. S. Reddy and J. S. Yadav, *Tetrahedron Lett.*, 2001, **42**, 3955–3958.
- 37 J. Klinowski, F. A. A. Paz, P. Silva and J. Rocha, *Dalton Trans.*, 2011, **40**, 321–330.
- 38 T. Kottke and D. Stalke, *J. Appl. Crystallogr.*, 1993, **26**, 615–619.
- 39 APEX2, *Data Collection Software Version 2.1-RC13*, Bruker AXS, Delft, The Netherlands, 2006.
- 40 Cryopad, *Remote Monitoring and Control, Version 1.451*, Oxford Cryosystems, Oxford, United Kingdom, 2006.
- 41 SAINT+, *Data Integration Engine v. 7.23a* ©, Bruker AXS, Madison, Wisconsin, USA, 1997–2005.
- 42 G. M. Sheldrick, *SADABS v.2.01, Bruker/Siemens Area Detector Absorption Correction Program*, Bruker AXS, Madison, Wisconsin, USA, 1998.
- 43 (a) G. M. Sheldrick, *SHELXS-97, Program for Crystal Structure Solution*, University of Göttingen, 1997; (b) G. M. Sheldrick, *Acta Crystallogr., Sect. A: Found. Crystallogr.*, 2008, **64**, 112–122.
- 44 G. M. Sheldrick, *SHELXL-97, Program for Crystal Structure Refinement*, University of Göttingen, 1997.
- 45 K. Brandenburg, *DIAMOND, Version 3.2f, Crystal Impact GbR*, Bonn, Germany, 1997–2010.